NASA TECHNICAL MEMORANDUM

NASA TM X-1656

NASA TM X-1656

EFFECT OF MODEL FOREBODY SHAPE ON PERFORATED TUNNEL WALL INTERFERENCE

by Glenn A. Mitchell

Lewis Research Center
Cleveland, Ohio

NATIONAL AERONAUTICS AND SPACE ADMINISTRATION • WASHINGTON, D. C. • OCTOBER 1968

NASA TM X-1656

EFFECT OF MODEL FOREBODY SHAPE ON PERFORATED TUNNEL WALL INTERFERENCE

By Glenn A. Mitchell

Lewis Research Center
Cleveland, Ohio

NATIONAL AERONAUTICS AND SPACE ADMINISTRATION

For sale by the Clearinghouse for Federal Scientific and Technical Information
Springfield, Virginia 22151 – CFSTI price $3.00

ABSTRACT

A 0.73-percent blockage cylindrical body was tested in the 8- by 6-foot supersonic wind tunnel with several forebody shapes to determine the magnitude of wall interference effects on model pressure distributions. The test section Mach number was varied from 0.4 to 2.0, and the distribution of wall porosity was adjusted. The forebody shape variations included cones with half angles of 15^{o} and 42^{o}, and a tangent ogive with a length to diameter ratio of 3. Results were compared to data on a 10^{o} conical forebody from a previous test.

EFFECT OF MODEL FOREBODY SHAPE ON PERFORATED TUNNEL WALL INTERFERENCE

by Glenn A. Mitchell

Lewis Research Center

SUMMARY

A 0.73-percent blockage cylindrical body was tested in the 8- by 6-foot supersonic wind tunnel with several forebody shapes to determine the magnitude of wall interference effects on model pressure distributions. The test section Mach number was varied from 0.4 to 2.0, and the distribution of wall porosity was adjusted. The forebody shape variations included cones with half angles of 15° and 42°, and a tangent ogive with a length-to-diameter ratio of 3. Results were compared to data on a 10° half-angle conical forebody from a previous test. Principal disturbances were caused by (1) displacement of the terminal shock near sonic speeds, (2) wall reflection of the forebody bow shock wave, (3) excessive wall porosity near sonic speeds, and (4) nonuniform distribution of tunnel wall porosity.

INTRODUCTION

As discussed in reference 1, a transonic wind tunnel design is a compromise of conflicting requirements resulting from the mutual interaction of the test model flow field and the tunnel walls. With a given tunnel design, there is a continuing motivation to utilize test models which are as large as possible without incurring serious compromises in flow quality. In some cases (e.g., aircraft aerodynamic force tests) only minor compromises are permissible. But in other cases, major compromises are essential or else tunnel test plans must be abandoned simply because the model is too small to satisfy other test requirements. Some examples of the latter situation include structural tests of full scale components of flight vehicles, dynamic tests of aeroelastic models of flight vehicles, model tests of complex variable geometry aircraft inlet and exhaust systems, or model tests wherein mixing and/or combustion phenomena are of fundamental interest as in launch vehicle base heating studies.

When interpreting results of tests requiring the use of large models, a general knowledge of the deviations in flow quality is needed to avoid inaccurate conclusions. However, only limited data have been published defining the consequences of using large models in transonic tests. For this reason, a series of calibration models have been tested in the Lewis 8- by 6-foot supersonic wind tunnel over its speed range from Mach 0.4 to 2.0. Results of varying the diameter of 10^{o} half-angle cone-cylinder models from 4 inches (10.16 cm) to 16 inches (40.64 cm) are reported in reference 2. In the present investigation, the cylinder diameter was fixed at 8 inches (20.32 cm) and the forebody shape was varied. Although some details of the results may be peculiar to the particular tunnel in which the tests were made, general trends may be expected to exist in other transonic tunnels of similar design.

SYMBOLS

D	diameter
L	length of ogive
M	Mach number
P	total pressure
p	static pressure
q	dynamic pressure
Δ	deviation

Subscripts:

aft	tunnel wall location at aft end of test section, station 13.8
b	base
max	maximum
0	free stream

APPARATUS AND PROCEDURE

Consideration in Selecting a Test Model

A determination of the tunnel flow quality can best be accomplished by comparing experimental pressure distributions obtained from a test body in the tunnel to theoretical pressure distributions. Such a comparison determines tunnel-originated disturbances

and measures the test section capability of handling supersonic and transonic interference phenomena. The effect of forebody shape on interference phenomena can be determined by testing models of constant maximum diameter, but with various forebody shapes.

The 8- by 6-foot supersonic wind tunnel is chiefly a propulsion research facility wherein a variety of combustion tests and variable geometry inlet and exhaust nozzle tests are conducted. Because of scale constraints required for this type of work, a majority of the test models are about 8 inches (20.32 cm) in diameter and have a model to tunnel blockage ratio of 0.73 percent. Therefore, an 8-inch (20.32-cm) cylinder was selected which utilized various forebody shapes and was sting mounted in the test section. Results obtained with a 10° half-angle cone are reported in reference 2. The additional forebodies of this study included 15° and 42° half-angle cones and a tangent ogive with a length-to-diameter ratio of 3. Theoretical pressure distributions for the 15° cone and for the ogive were obtained from references 3 and 4, respectively. Where appropriate, these theoretical distributions were extrapolated to lower Mach numbers. The 42° cone was selected to provide bow shock detachment over the range of test Mach numbers to present a severe test of the tunnel wall wave cancellation characteristics. Theoretical pressure distributions were not available; and, hence, only a qualitative examination of these pressure distributions was appropriate.

Considerations in Varying Test Sections

The 8- by 6-foot supersonic wind tunnel was originally designed to operate in the speed range from Mach 1.5 to 2.0. Subsequently, the test section walls were perforated to permit transonic operation. The perforation design was based on the differential resistance concept of reference 5. One-inch (2.54-cm) diameter holes were drilled in the 8- by 6-foot tunnel wall inclined 60° from the normal. They provide greater resistance to inflow than to outflow and thereby minimize the strength of wall-reflected disturbances from the model flow field. General arrangement of the test section equipment is illustrated in figure 1(a).

In this particular tunnel the perforations are arranged in a herringbone pattern which is inclined 75° to the flow direction and is symmetrical about the center of each wall. Although the objective in design of the wall perforations was to provide a uniform porosity of 6 percent over a 14-foot (4.27-m) length, existing support structure limited hole placement and resulted in large wall areas without porosity. Although an average porosity of 5.8 percent was achieved, nearly 50 percent of the wall area was unperforated and local porosity in the perforated regions was 11.2 percent.

Results of reference 2 showed advantages of blocking some of the perforations. During the current series of tests only the 8-foot (2.44-m) test section was used with either

an average porosity of 6.2 or 3.1 percent. The resulting distribution of porosity is shown in figure 1(b). Limited data were also obtained with a modified 8-foot (2.44-m) test section wherein some perforations were opened on the floor and ceiling plates upstream of the 8-foot (2.44-m) test section. The intent was to initiate the plenum suction controlled Mach number upstream of the test model and prevent any Mach number gradient originating at the start of perforations from impinging on the test model. Although these disturbances are slight with proper setting of plenum chamber pressure, the accuracy in control of this pressure is less critical with the additional length of the modified test section. The porosity of this modification is also shown in figure 1(b).

The combinations of model and test section configurations is summarized in table I. Schematic drawings of the test models and of their placement in the test section are shown in figure 2.

Instrumentation

All test models were instrumented with two rows of static pressure taps: one row in the horizontal plane and the other in the vertical plane. The taps were generally 2 inches (5.08 cm) apart, but were spaced as close as 1 inch (2.54 cm) immediately aft of the forebody-cylinder juncture. The models were also instrumented with four base pressure taps. A longitudinal row of static pressure taps along the tunnel side wall and top wall were used as an aid in tracing and interpreting the various disturbances which were encountered. Total pressure was measured in the tunnel bellmouth forward of the flexible nozzle and was corrected by a previously calibrated loss factor to obtain the test section total pressure. The pressure in the plenum chamber surrounding the test section was measured and ratioed to the free-stream total pressure to yield test section Mach number through a previous calibration.

Selection of Optimum Operating Conditions

The Mach number in the transonic test section of the tunnel was varied during these tests from 0.40 to 2.0 in approximate intervals of 0.1 Mach number by proper setting of four controls: compressor speed, flexible nozzle position, plenum chamber suction, and second throat position. In the supersonic speed range (Mach 1.1 to 2.0) the second throat was positioned open and the compressor speed was governed by a requirement of sufficient pressure ratio for supersonic flow. The flexible nozzle was used to set the Mach number entering the perforated test section. Vernier adjustments to the Mach number within the perforated test section were made by varying the plenum chamber suction flow rate to obtain a series of data points in each 0.1 Mach number interval. These

data were used to select (on the basis of the best body pressure distributions) the optimum plenum pressures for each test section configuration. The data presented herein are the closest available test points to these optimum conditions. At subsonic speeds, the flexible nozzle was not a useful variable and was left in a wide-open position. Plenum chamber flow rate, second throat position, and compressor speed were all capable of varying the subsonic Mach number. Optimum settings of plenum chamber suction and second throat position were determined from data obtained during the current test. Unique values of compressor speed were then required at each Mach number in order to prevent unloading of the last stages of the compressor and overpressurization of the plenum chamber surrounding the test section.

DISCUSSION OF RESULTS

Pressure Distributions

Zero degree angle of attack pressure distributions were obtained on the model surfaces for the model and test section configurations shown in table I. The pressure distributions for most of these configurations are presented in figures 3 to 7. Results for the 15° half-angle cone and the ogive forebodies in the 8 foot (2.44 m) - 3.1 percent porosity test section are not shown, since they were similar to those in the modified 8 foot (2.44 m) - 3.1 percent porosity test section. The 10° cone pressure distributions are presented in reference 2. Data are shown in each figure in order of increasing Mach number over the complete speed range investigated for each configuration. At the subsonic Mach numbers where theoretical pressure distributions were not available, the tunnel static pressure level is shown at the end of each pressure distribution. At higher Mach numbers, the theoretical pressure distributions are shown as the solid lines. Judicious extrapolations of theoretical pressure distributions to sonic speeds are also shown as solid lines.

Transonic and Supersonic Flow Disturbances

All major flow disturbances occurring at transonic and supersonic Mach numbers were traceable to a known source. These are identified in figures 3 to 7. The distortion of the model surface pressures resulting from the various flow disturbances was obtained from figures 3 to 7 and reference 2. Figure 8 presents the pressure distortion as a function of Mach number to obtain a comparison of the effects of forebody shape on the flow quality in each test section. In reference 2 the effects of model size were determined by

comparing the magnitude of the maximum pressure deviation above or below the theoretical curve. This technique sufficed because the models were similar; each having a 10^{o} cone. Because the models to be compared herein have various forebody shapes and create dissimilar flow fields, a new parameter, distortion, was chosen to yield a valid comparison. The magnitude of the pressure distortion was defined as the sum of the maximum positive and negative experimental pressure deviations from the theoretical curve or, where applicable, from the extrapolated curve. Since the theoretical distributions were not available for the 42^{o} cone, the distortion was obtained from the deviations above and below the general average pressure level that existed on the cylinder aft of the cone juncture region.

In all cases, the maximum distortion existed at Mach 1.1. The distortion magnitude increased as cone angle increased; and in virtually all cases, the ogive distortion was the least of all.

These results are replotted in figure 9 to more clearly indicate the effect of the test section configuration. The 3.1-percent porosity test section was superior at Mach numbers less than 1.3, but at higher speeds there was little difference. Only minor differences are apparent between the 8-foot (2.44-m) test section and the modified 8-foot (2.44-m) test section, but it should be noted that in all cases the plenum chamber pressure was set carefully to avoid disturbances at the start of perforations and hence the advantages of the modified test section would not be apparent.

The effect of forebody shape and test section variation on each of the major flow disturbances was determined from the pressure distributions of figures 3 to 7 and reference 2, and is presented in figures 10 to 18. Because a specific disturbance was compared, the magnitude was defined as the simple deviation in pressure from the theoretical curve, or in the case of the 42^{o} cone, the deviation from the average pressure level.

The terminal shock. - In free flight at transonic speeds, a terminal shock exists aft of the forebody-cylinder juncture on bodies similar to those tested herein. It occurs because there is a local overexpansion of the flow near the juncture to supersonic speeds and the flow is evidently unable to recompress back to the subsonic free-stream static pressure without generating a shock (ref. 6). As the flight velocity increases, the terminal shock moves rapidly aft and disappears downstream at speeds slightly above Mach 1. In the presence of the tunnel wall, however, the flow field is radically altered about a body of large blockage and so is the terminal shock location. According to reference 7, the location of the terminal shock is believed to be linked to the intersection of the expansion field from the model with the tunnel walls. The progression of this disturbance through the transonic speed range is evident in each of the pressure distributions of figures 3 to 7. In figure 10 the terminal shock location is shown as a function of Mach number for each model shape tested. Also shown for reference are shock locations for a 0.005-percent blockage model as obtained from schlieren photographs of reference 7.

These data were presumed to be representative of flight because of the small model size. Large models severely retard the aft movement of the terminal shock with increasing Mach number and, hence, posed a serious departure from free-flight simulation. As shown in reference 2, the model size (or blockage) is a major factor affecting this displacement of the terminal shock position. However, figure 10 indicates that there are only minor effects of forebody shape and test section configuration.

The effect of model forebody shape on terminal shock magnitude is shown in figure 11. The ogive model terminal shock was generally the weakest and that of the cone models generally increased as the cone angle increased. These results are replotted in figure 12 to show the effect of tunnel wall porosity. The 3.1-percent porosity consistently produced lower shock strength, and again there was little difference between the 8-foot (2.44-m) test section and the modified version.

Nose shock wave reflection. - With the 10° cone models of reference 2, it appeared that the conical shock wave was effectively canceled by the perforated tunnel wall. With the blunter models of this test, wall reflection to the model became apparent. It was evident with all configurations at Mach numbers of 1.2 or greater (figs. 3 to 7). However, it was a relatively minor disturbance except for conditions where it reflected from the unperforated region at station 9.5. The magnitude of the wall reflected nose shock is summarized in figure 13. There seemed to be relatively little variation between models considering the large variations in bluntness. The shock reflection from the ogive, with an initial angle of 18.9°, was weaker than for the 15° cone. These results are replotted in figure 14 to show the effect of test section configuration. The only significant difference occurred for the bluntest model (42° cone) for which the 6.2-percent porosity test section provided better performance than the 3.1-percent porosity test section.

Excessive wall porosity at low supersonic speeds. - Nose shock reflection as a compression wave was only apparent at Mach numbers of 1.2 or higher. However, it was observed that the forebody compression field reflected from the wall as an expansion wave at lower speeds near Mach 1.1. An example of the disturbance caused by this overexpansion is shown in figures 3(g) and (h). It was most prominent at Mach numbers near 1.1, but decreased rapidly as the Mach number increased to 1.2 or higher. References 2 and 8 indicate that this overexpansion is a consequence of excessive wall porosity at low supersonic speeds. The effect of forebody shape on the magnitude of the overexpansion is summarized in figure 15. The only marked difference between the various shapes was that the 42° cone disturbance exceeded the general level of the others. Effects of test section geometry are summarized in figure 16. The low (3.1 percent) porosity tunnel reflected the smallest overexpansion, but the differences were not large.

Unperforated wall near station 9.5. - A porosity deficit at tunnel station 9.5 (fig. 1(b)) existed because of external vertical support beams of the tunnel structure. A disturbance from this region was observed propagating along the Mach angle to the model

from both the tunnel horizontal and vertical walls. Since this disturbance was essentially a solid wall reflection of waves originating from the model, it existed at supersonic speeds and depended upon the nature of the incident wave. Examples are shown in figure 3 at Mach numbers from 1.101 to 1.766. Disturbance magnitudes are summarized in figure 17. The effect of varying forebody shape was generally inconsistent. This resulted because the reflected waves were not only affected by forebody shape and Mach number, but also depended upon the flow field each model presented to the unperforated region. For example, the expansion field emanating from the juncture of the model forebody and cylinder was different in location and strength for each model. As shown in figure 18, there was little difference for varying test section configurations.

Subsonic Flow Acceleration

As was explained in reference 2, the flow at the aft end of the transonic test section tended to accelerate at subsonic speeds. This was reflected as a decrease in aft end tunnel pressures and in pressures on models located near the end of the test section. For example, in figures 3 to 7, the subsonic pressure distributions within 25 inches (63.5 cm) of the model base are affected to varying degrees by a pressure gradient at the aft end of the test section. These data were obtained prior to finding optimum tunnel settings which corrected the gradient. The 15° half-angle cone and the ogive forebody pressure distributions were close to the optimum settings and exhibit a slight pressure decrease near the model base. The data of the 42° cone-cylinder were farther from optimum and show a larger drop in pressure.

Control of the aft end flow acceleration has been gained by varying the tunnel second throat in conjunction with the plenum chamber suction. Varying these parameters at a given subsonic Mach number resulted in a change in the longitudinal tunnel static pressure gradient. The effect of this gradient, $(p_{aft} - p_0)/q_0$, on the pressure distributions of an aft located model is illustrated in figure 19. Pressures on models located at a more upstream location are unaffected by the tunnel static pressure gradient. The single pressure profile illustrated at the upstream base location of figure 19 is typical for a sting-mounted cylindrical afterbody. The pressure drop near the base results from the subsonic flow acceleration around the sharp base edge.

Utilization of the aft end of the test section for model testing was obtained by establishing an acceptable setting of the longitudinal static pressure gradient. Reference 9 had indicated that model base pressure was the most sensitive indication of the effects of gradients at the rear of the test section. Various gradients were set for each subsonic Mach number, and model base pressures for both the ogive-cylinder and the 15° cone-cylinder were recorded for both upstream and downstream model locations. The result-

ing data are shown in figure 20 for both the 14-foot (4.27 m) and the 8-foot (2.44 m) test sections. Model forebody variations had no effect on the data and are not identified on the figure. As expected, the base pressures at the upstream locations were barely affected by variations of the pressure gradient, whereas the aft-located base showed large pressure variations. It was assumed that the minimum gradient was established at the tunnel centerline when the base pressures at the aft location matched those at the upstream location. Thus, the recommended pressure gradient settings shown in figure 21 were generated. The technique used here was similar to that of reference 9.

SUMMARY OF RESULTS

Pressure distributions were obtained on 8-inch (20.32-cm) diameter cylinders which utilized a variety of forebody shapes in the 8- by 6-foot supersonic wind tunnel. Perforated tunnel wall interference effects were determined in the speed range Mach 0.4 to 2.0. Forebody shapes included 15° and 42° half-angle cones, and a tangent ogive with a length-to-diameter ratio of 3. These results were compared to data from a 10° conical forebody of a previous study. Variations in tunnel wall perforations were made to obtain average porosities of 3.1 and 6.2 percent. The following results were obtained:

1. The maximum interference effect occurred at Mach 1.1. Its magnitude was least for the ogive model and increased as the cone angle increased. It also was less with the lower porosity wall.

2. Displacement of the terminal shock position was relatively insensitive to the forebody shape and wall porosity changes. Its magnitude was least for the ogive model and increased as the cone angle increased. Shock amplitude was less with the lower porosity wall.

3. Nose shock reflection was not detected with the 10° cone, but was observed with the blunter forebodies. Its magnitude was not strongly dependent on the shape of the blunter bodies but tended to be weaker with the ogive. The higher porosity wall was effective in minimizing its strength with the bluntest forebody (42° cone).

4. The forebody compression field reflected from the wall as an expansion at Mach numbers near 1.1. Its disturbance magnitude was reduced by decreasing porosity.

5. Reflected disturbances from unperforated wall regions lateral to the flow direction were not altered by varying test section porosity.

6. Proper setting of the tunnel second throat and plenum chamber suction corrected subsonic flow acceleration at the aft end of the test section and allowed use of the more aft portions of the tunnel.

Lewis Research Center,
National Aeronautics and Space Administration,
Cleveland, Ohio, April 23, 1968,
720-03-01-08-22.

REFERENCES

1. Goethert, Bernhard H.: Transonic Wind Tunnel Testing. AGARDograph No. 49, Pergamon Press, 1961.
2. Mitchell, Glenn A.: Blockage Effects of Cone-Cylinder Bodies on Perforated Wind Tunnel Wall Interference. NASA TM X-1655, 1968.
3. Clippinger, R. F.; Giese, J. H.; and Carter, W. C.: Tables of Supersonic Flows About Cone Cylinders. Part 1: Surface Data. BRL Rep. No. 729, Aberdeen Proving Grounds, July 1950.
4. Dunn, Eldon L.: Some Results of a Systematic Theoretical Pressure Distribution Program on Bodies of Revolution. Tech. Memo 919, U. S. Naval Ordnance Test Station, Apr. 8, 1953.
5. Chew, W. L.: Experimental and Theoretical Studies on Three-Dimensional Wave Reflection in Transonic Test Sections. Part III. Characteristics of Perforated Test-Section Walls with Differential Resistance to Cross-Flow. Aro, Inc. (AEDC TN 55-44), Mar. 1956.
6. Sinnott, Colin S.: On the Prediction of Mixed Subsonic/Supersonic Pressure Distributions. J. Aero/Space Sci., vol. 27, no. 10, Oct. 1960, pp. 767-778.
7. Page, William A.: Experimental Study of the Equivalence of Transonic Flow About Slender Cone-Cylinders of Circular and Elliptic Cross Section. NACA TN 4233, 1958.
8. Felix, A. Richard: Variable Porosity Walls for Transonic Wind Tunnels. Presented at the 22nd Semi-Annual Meeting of the Supersonic Tunnel Association, Brussels, Belgium, Sept. 1964.
9. Nichols, James H.: Determination of Optimum Operating Parameters for the PWT 16-Ft Transonic Circuit Utilizing One-Percent Bodies of Revolution. Aro, Inc. (AEDC TN-59-100), Sept. 1959.

TABLE I. - MODEL AND TEST SECTION CONFIGURATIONS

Models (8-in. (20.32-cm) diam, 0.73 percent blockage)	Test section								
	8 ft (2.44 m), 6.2 percent porosity			8 ft (2.44 m), 3.1 percent porosity			Modified 8 ft (2.44 m), 3.1 percent porosity		
	Model length								
	in.	cm	diam	in.	cm	diam	in.	cm	diam
10^{o} Half-angle cone-cylinder	86.4	219.5	10.8	86.4	219.5	10.8	-----	------	----
15^{o} Half-angle cone-cylinder	-----	-----	----	86.4	219.5	10.8	86.4	219.5	10.8
Ogive cylinder, L/D = 3	87.47	222.17	10.9	87.47	222.17	10.9	87.47	222.17	10.9
42^{o} Half-angle cone-cylinder	86.4	219.5	10.8	86.4	219.5	10.8	-----	------	----

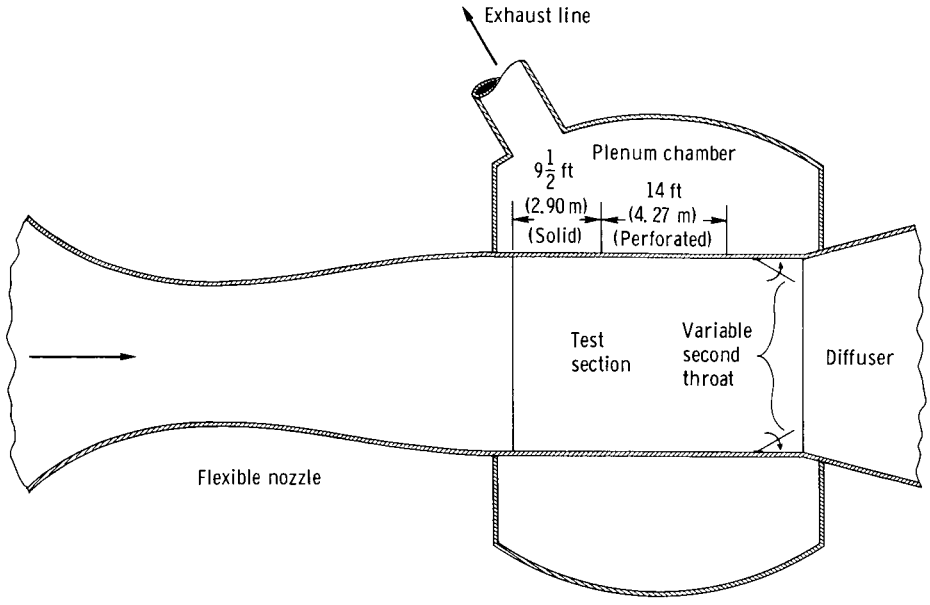

(a) Schematic drawing of test section and associated equipment.

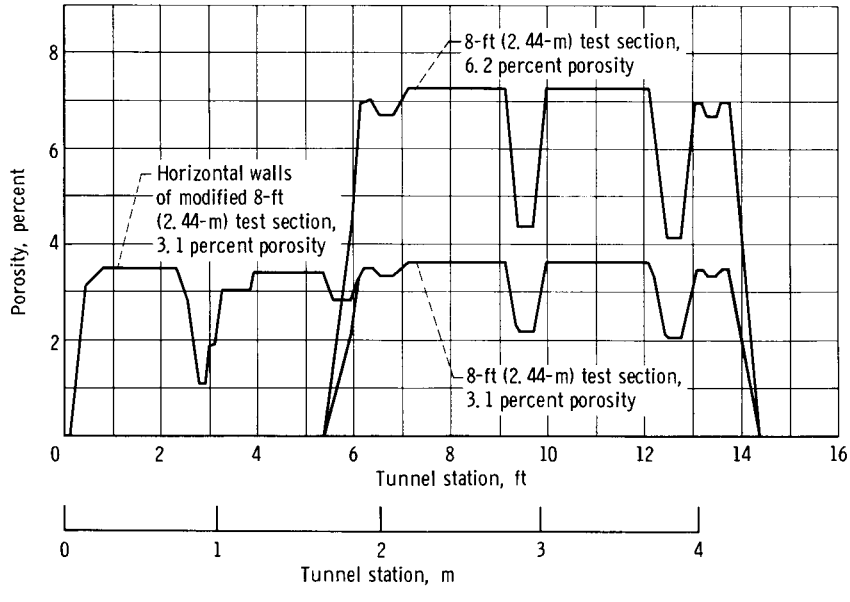

(b) Distribution of porosity.

Figure 1. - The 8- by 6-foot supersonic wind tunnel test section design.

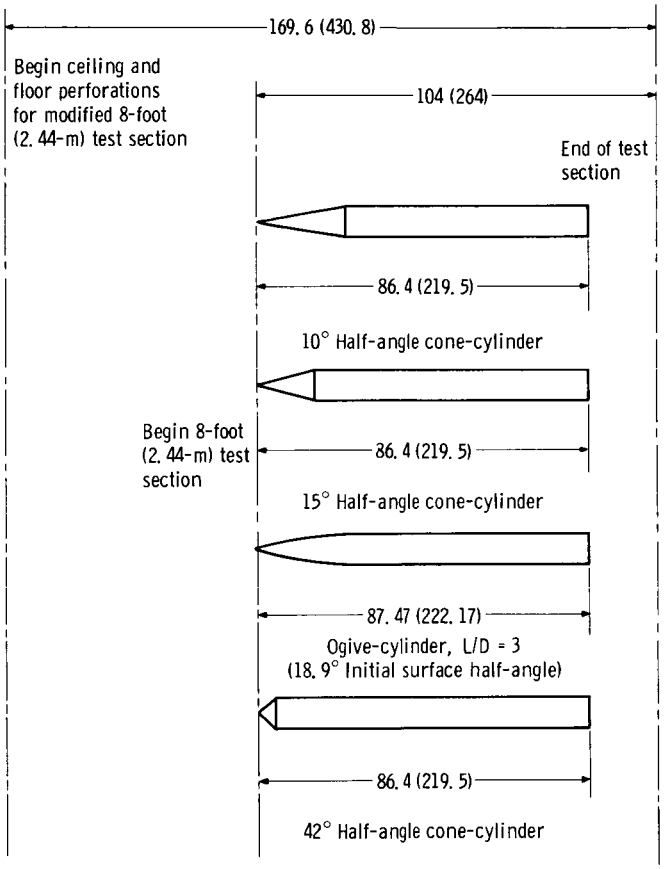

Figure 2. - Model dimensions and test locations. (Dimensions are in inches (cm).)

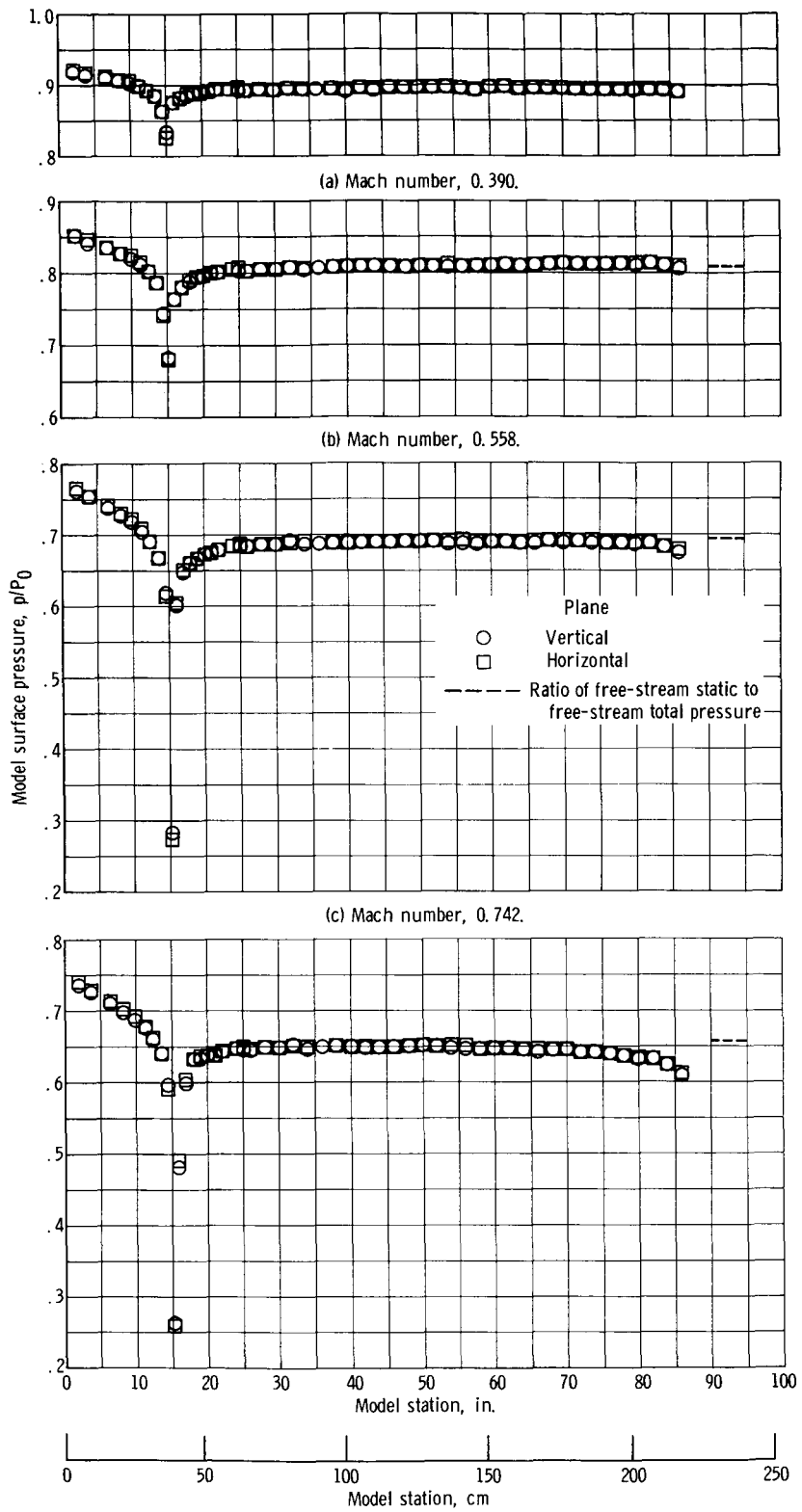

Figure 3. - Pressure distributions on 8-inch-diameter (20.32-cm-diam) 15° half-angle cone-cylinder model in modified 8-foot (2.44-m)-3.1 percent porosity test section.

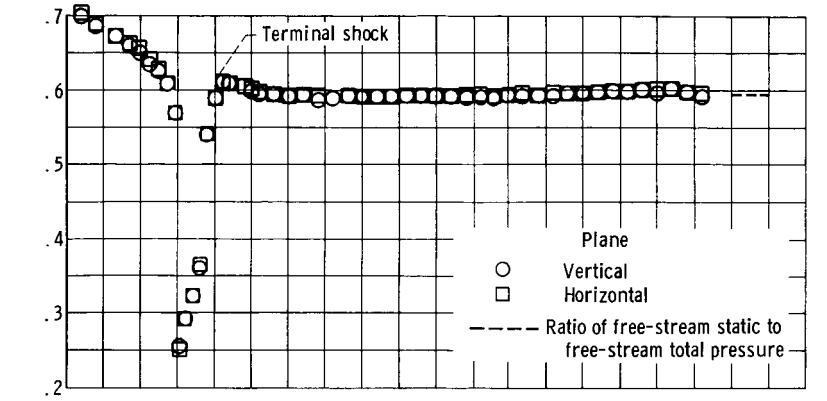

(e) Mach number, 0.895.

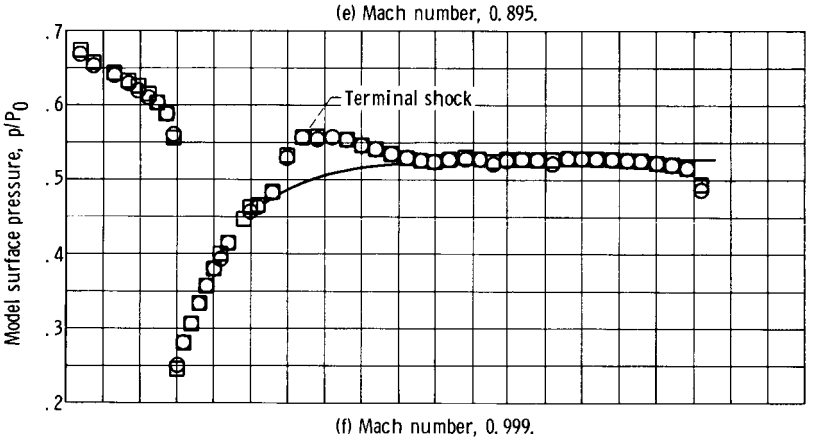

(f) Mach number, 0.999.

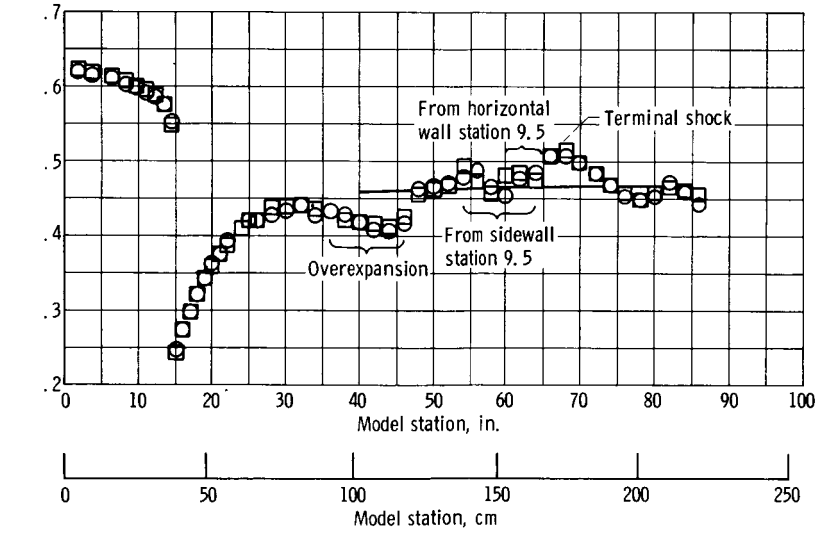

(g) Mach number, 1.101.

Figure 3. - Continued.

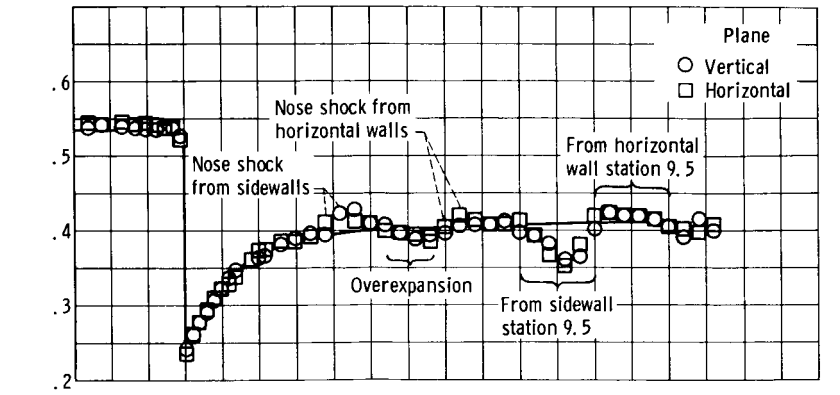

(h) Mach number, 1.204.

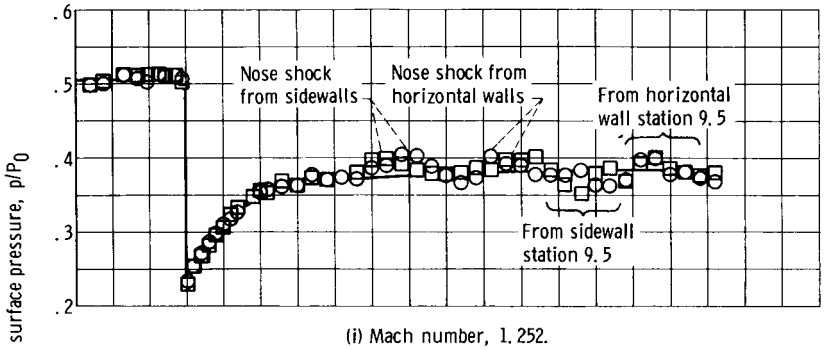

(i) Mach number, 1.252.

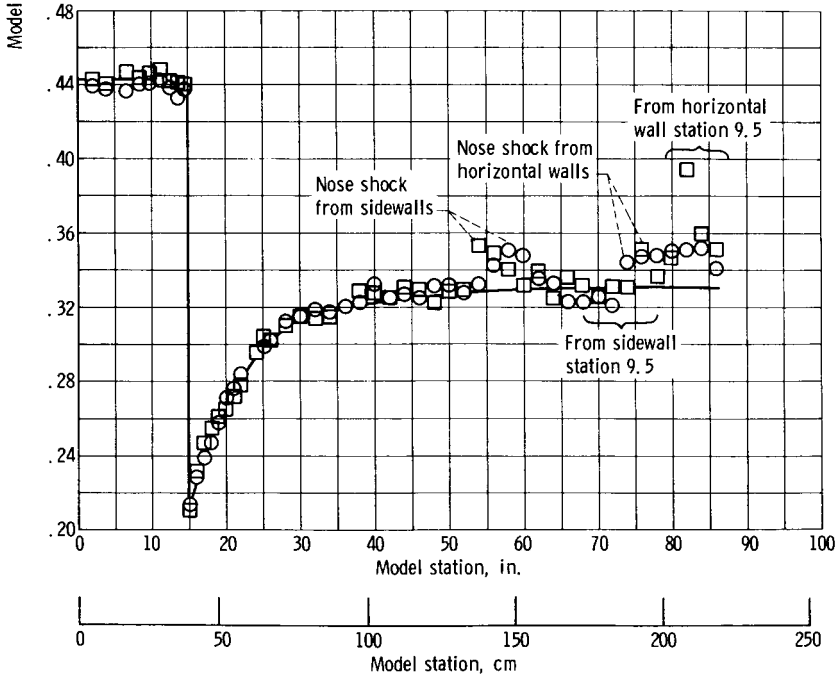

(j) Mach number, 1.362.

Figure 3. - Continued.

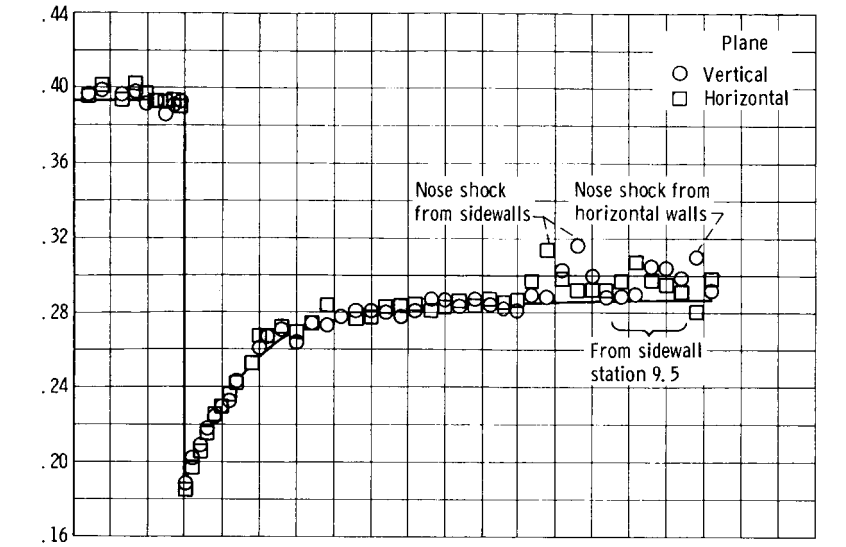

(k) Mach mach, 1.462.

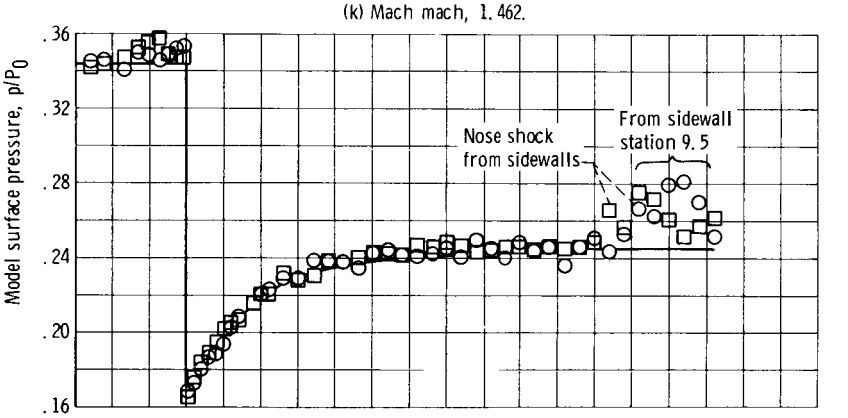

(l) Mach number, 1.569.

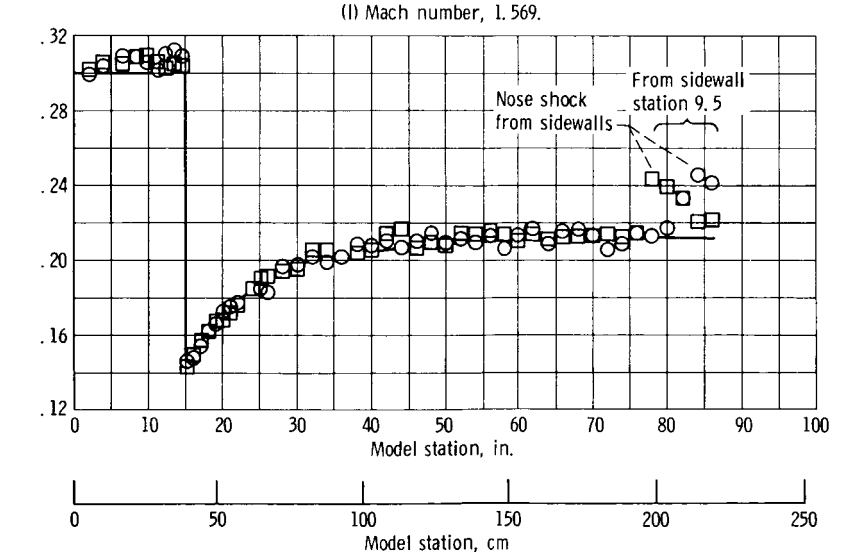

(m) Mach number, 1.668.

Figure 3. - Continued.

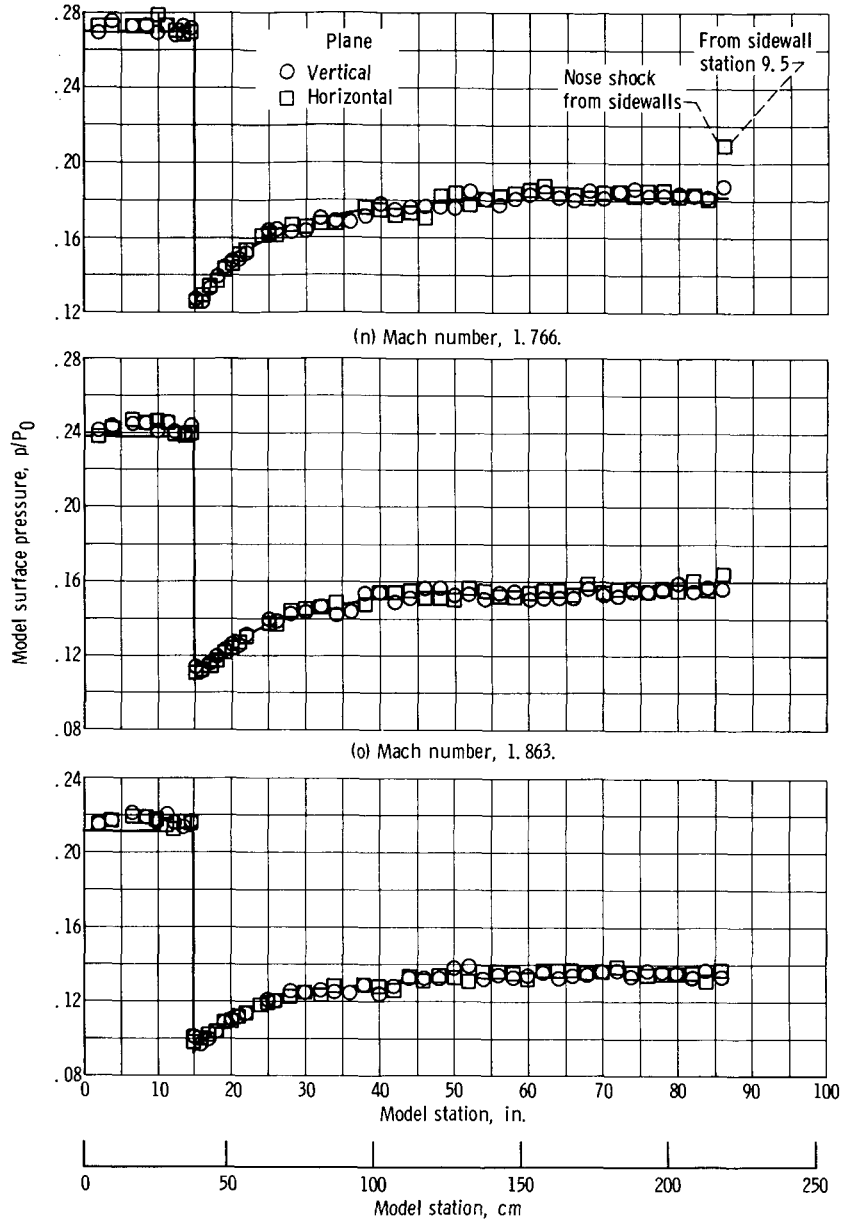

(n) Mach number, 1.766.

(o) Mach number, 1.863.

(p) Mach number, 1.956.

Figure 3. - Concluded.

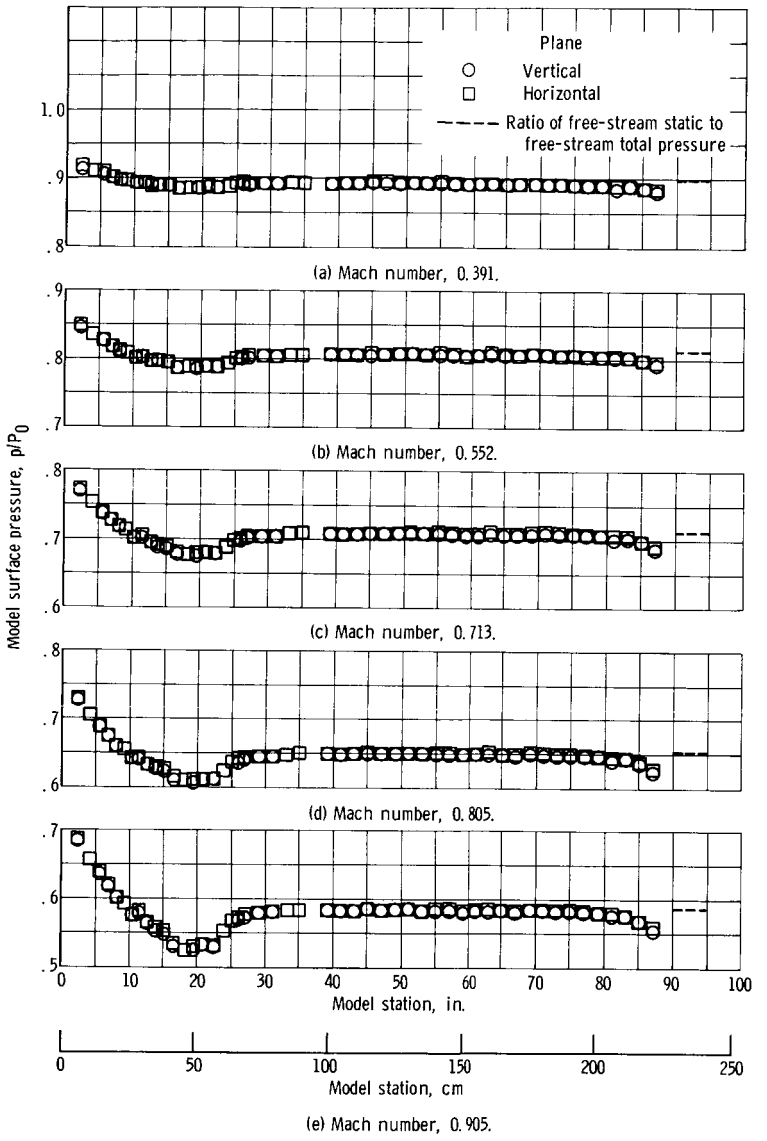

Figure 4. - Pressure distributions on 8-inch-diameter (20.32-cm-diam) L/D of 3 ogive-cylinder model in modified 8-foot (2.44-m) - 3.1 percent porosity test section.

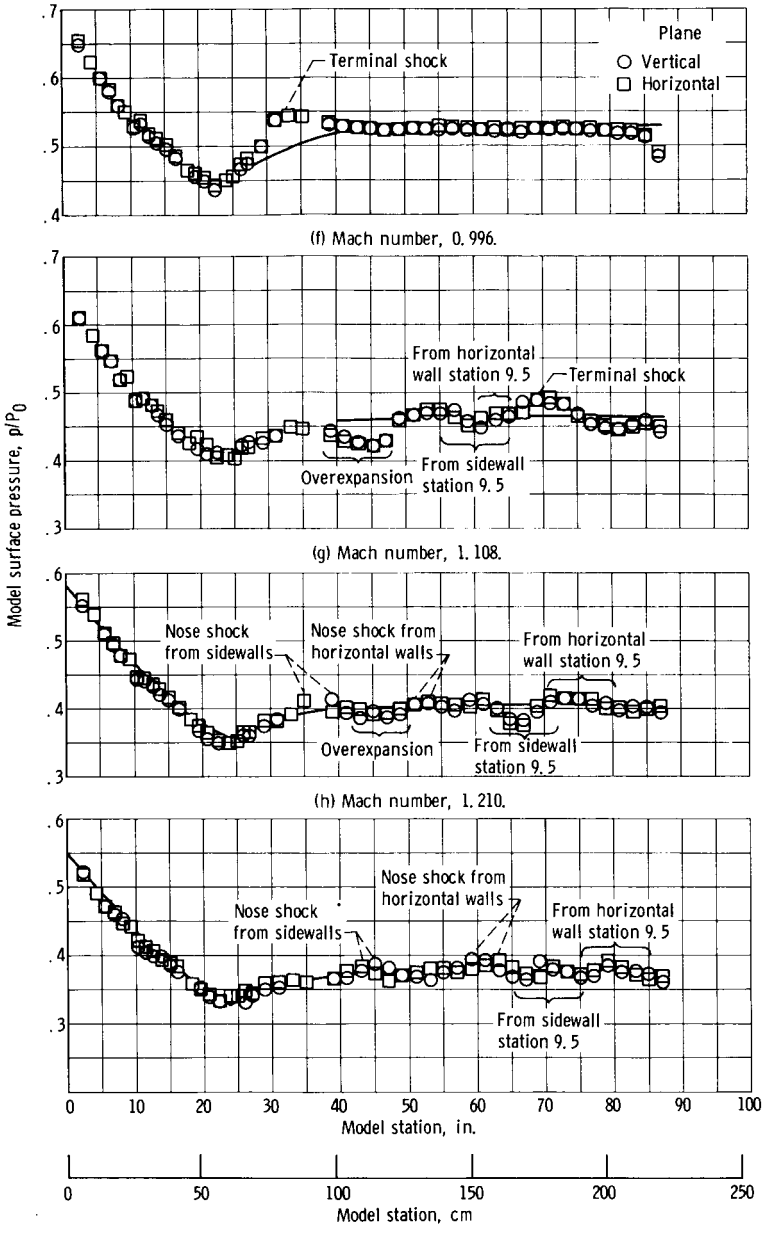

(f) Mach number, 0.996.

(g) Mach number, 1.108.

(h) Mach number, 1.210.

(i) Mach number, 1.264.

Figure 4. - Continued.

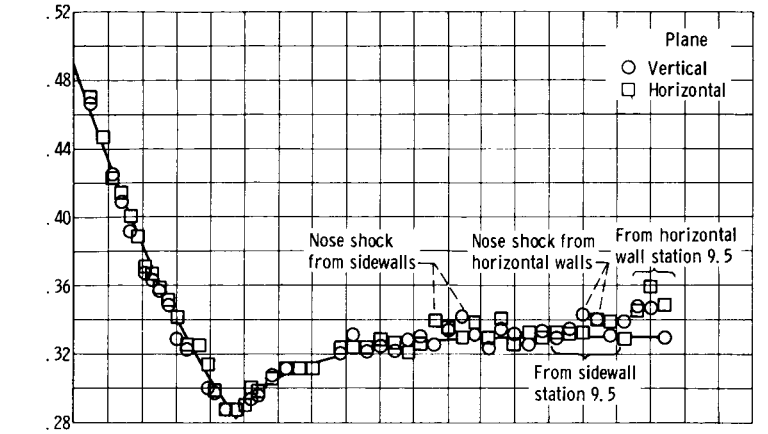

(j) Mach number, 1.365.

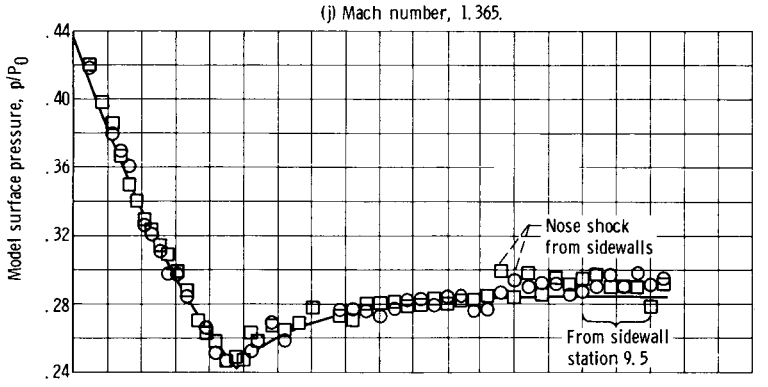

(k) Mach number, 1.470.

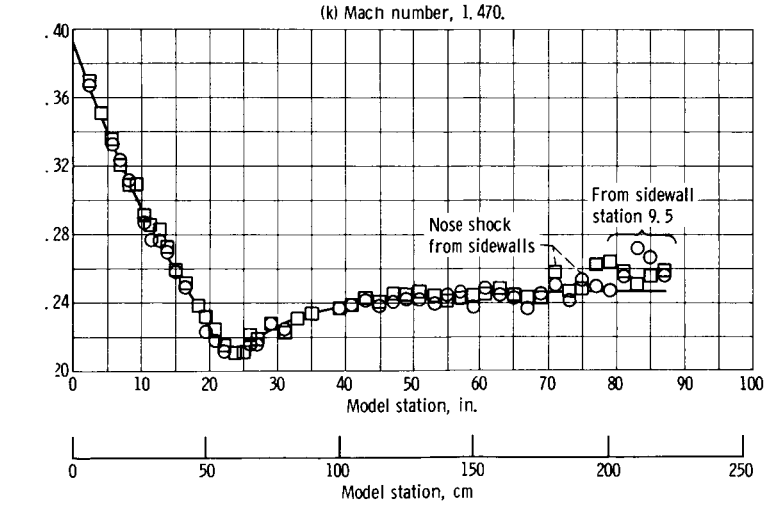

(l) Mach number, 1.569.

Figure 4. - Continued.

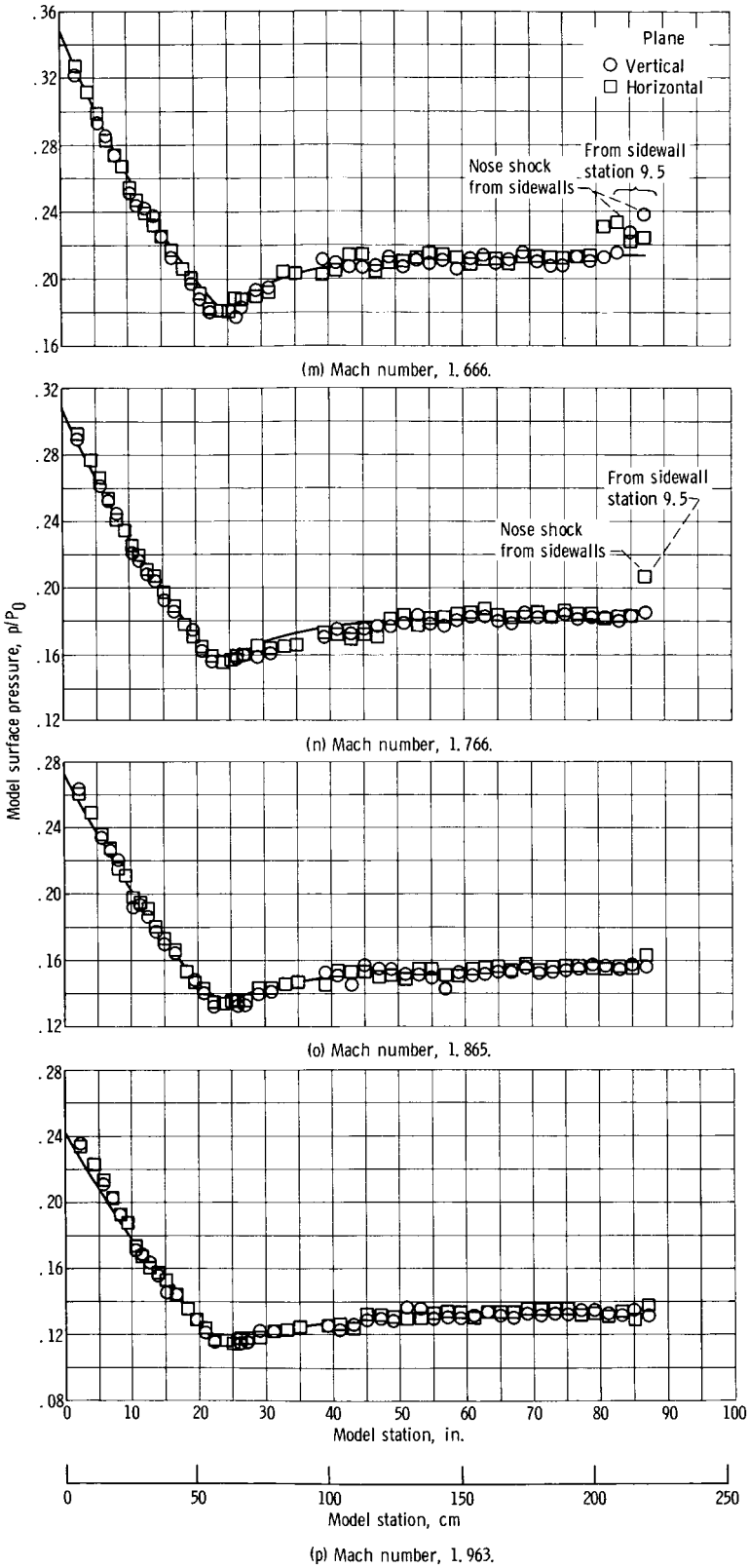

(m) Mach number, 1.666.

(n) Mach number, 1.766.

(o) Mach number, 1.865.

(p) Mach number, 1.963.

Figure 4. - Concluded.

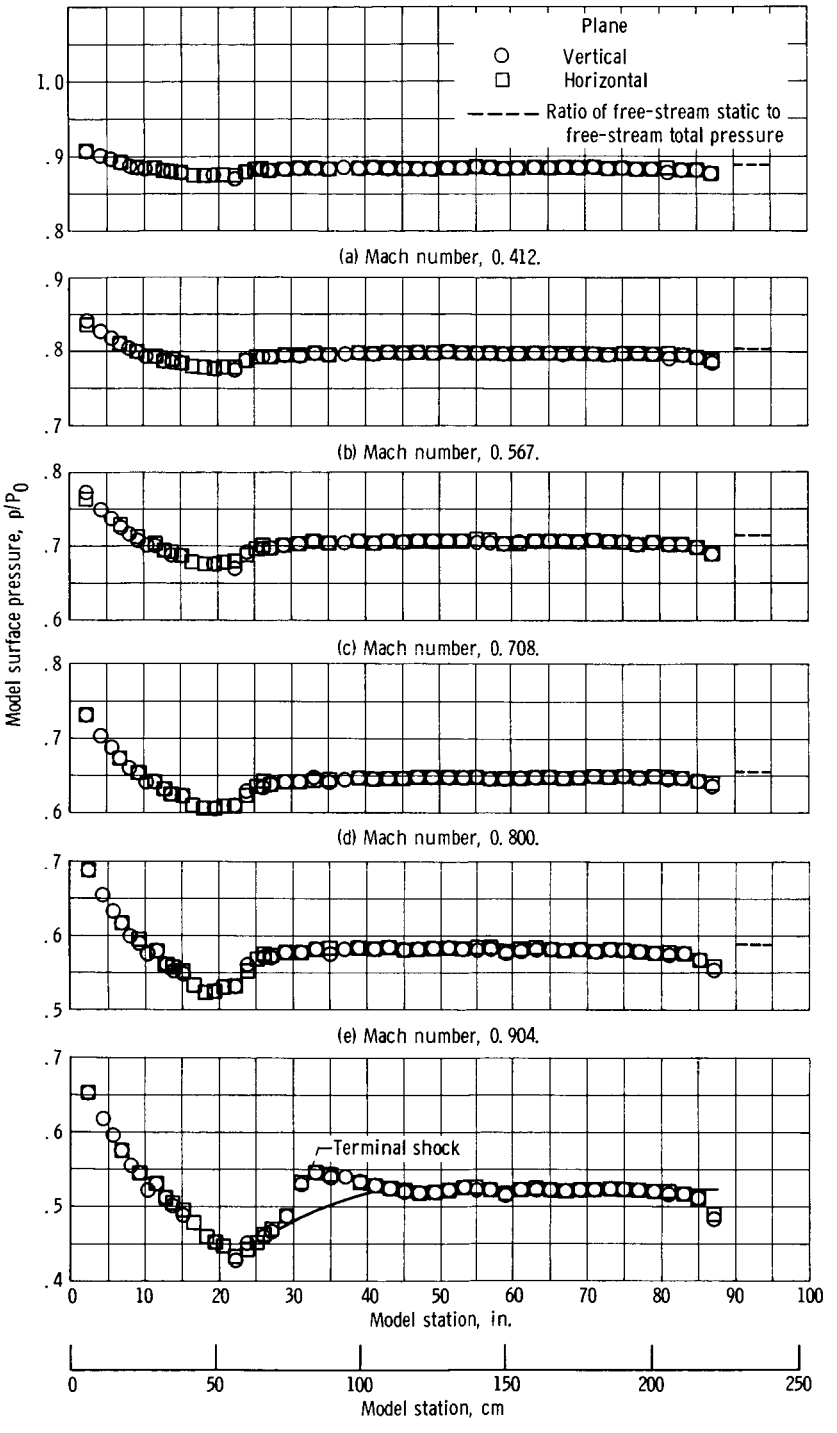

Figure 5. - Pressure distributions on 8-inch-diameter (20.32-cm-diam) L/D of 3 ogive-cylinder model in 8-foot (2.44-m) - 6.2 percent porosity test section.

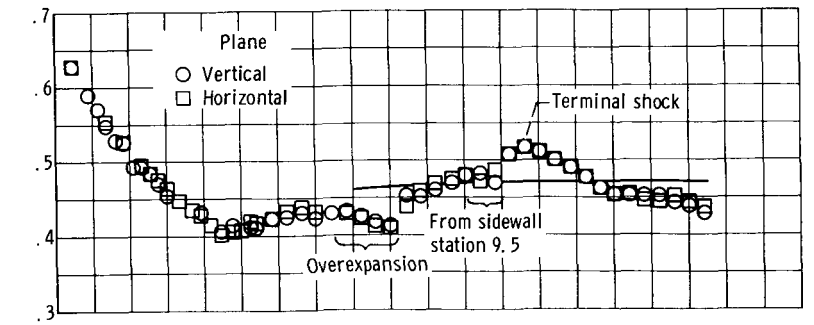

(g) Mach number, 1.099.

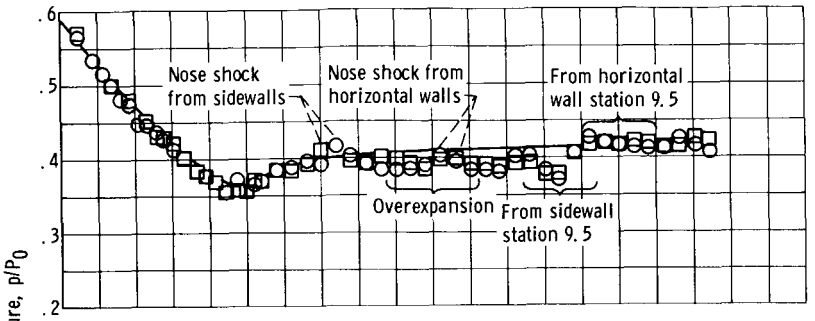

(h) Mach number, 1.200.

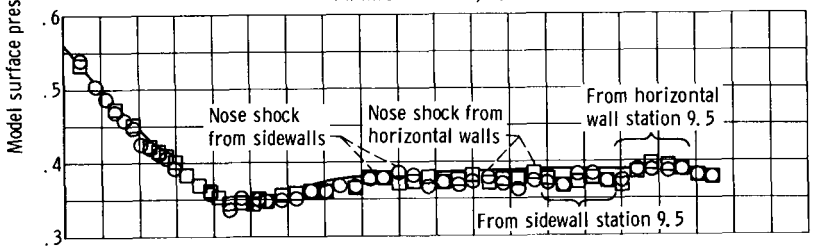

(i) Mach number, 1.245.

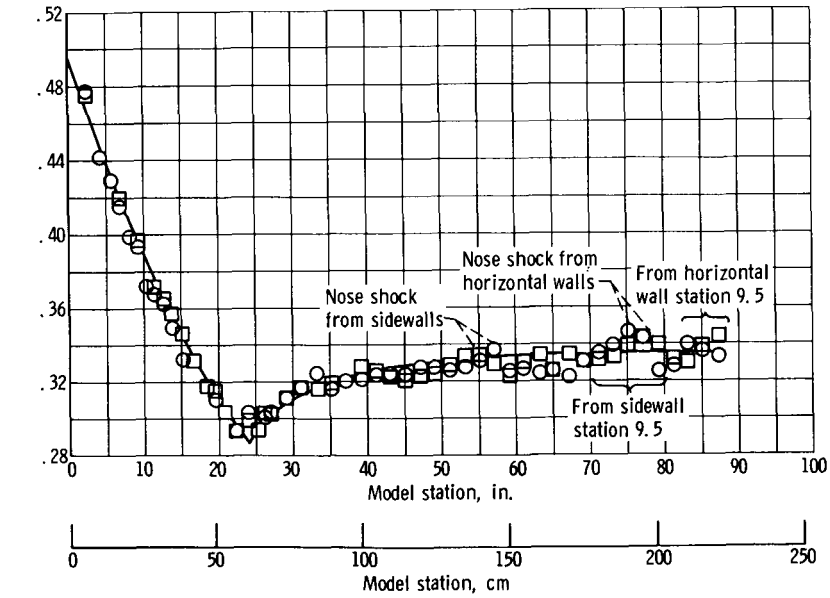

(j) Mach number, 1.356.

Figure 5. - Continued.

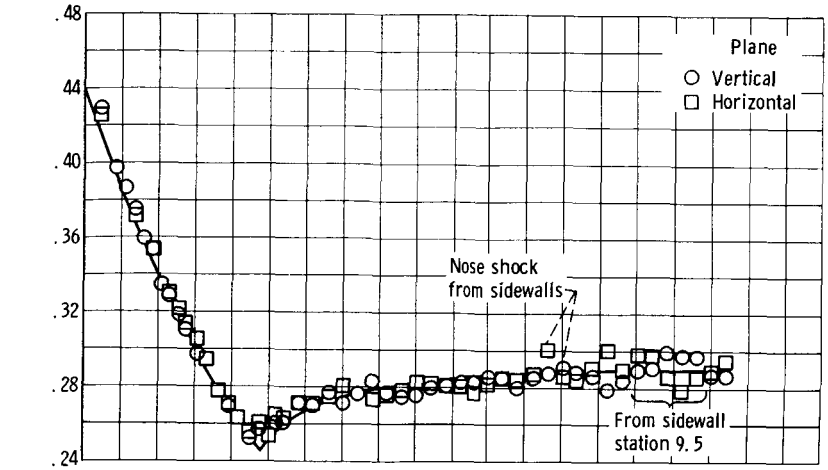

(k) Mach number, 1.459.

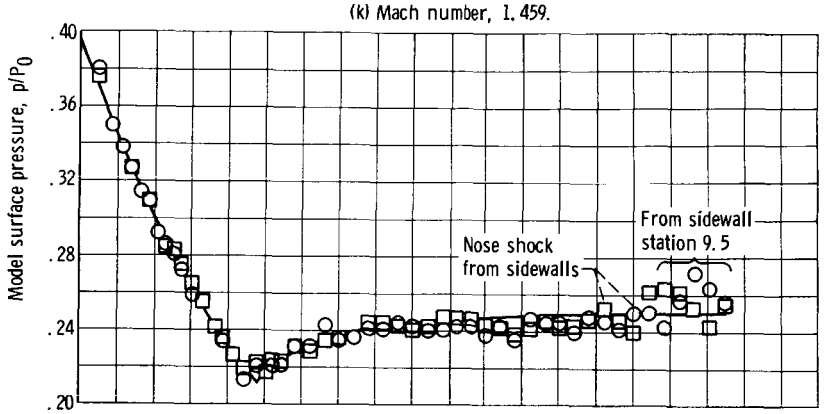

(l) Mach number, 1.560.

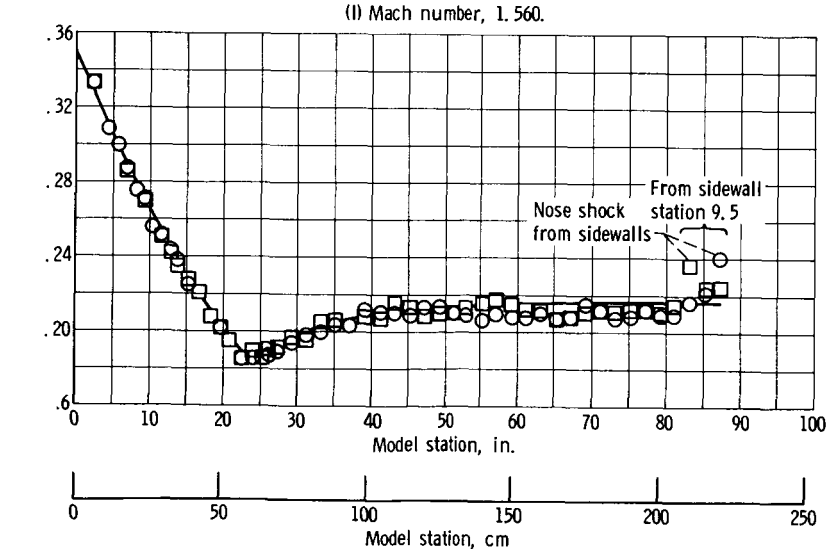

(m) Mach number, 1.659.

Figure 5. - Continued.

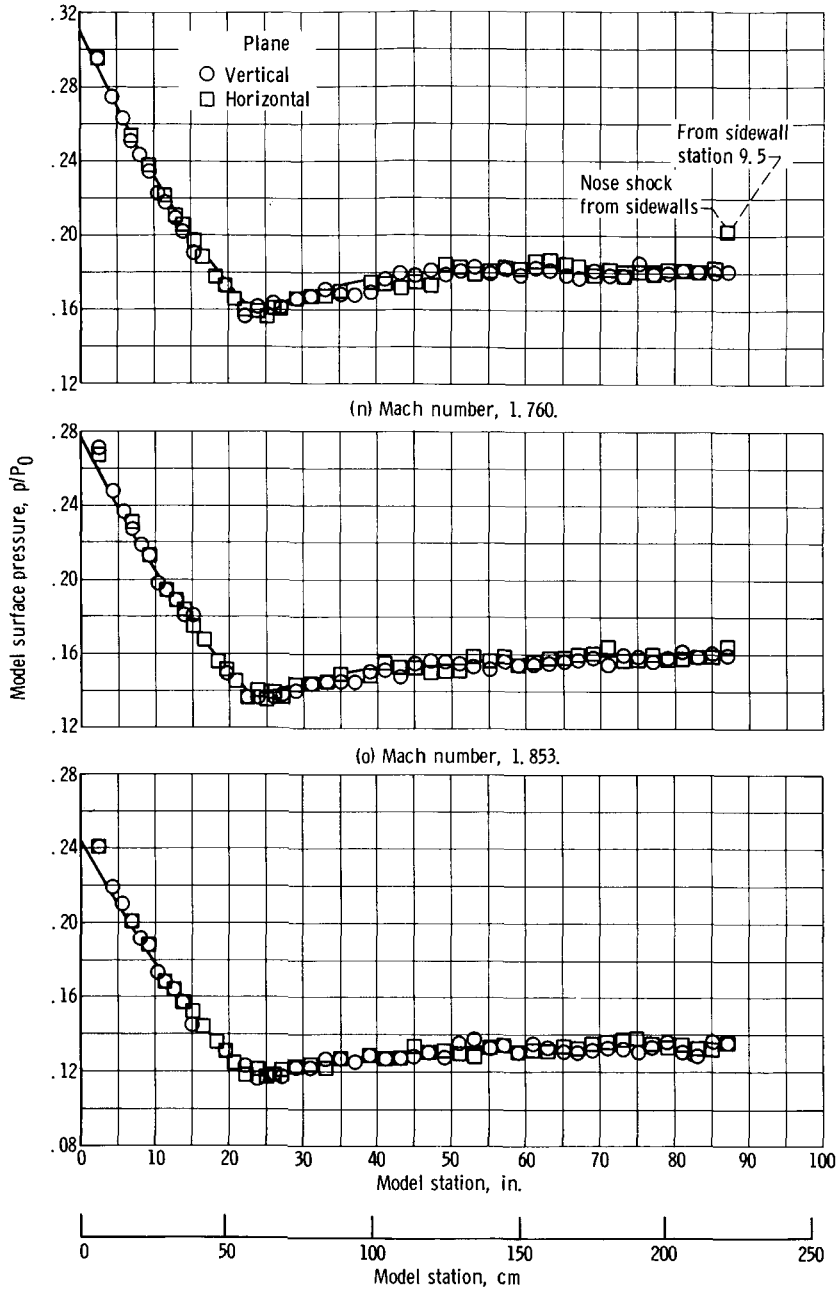

(n) Mach number, 1.760.

(o) Mach number, 1.853.

(p) Mach number, 1.956.

Figure 5. - Concluded.

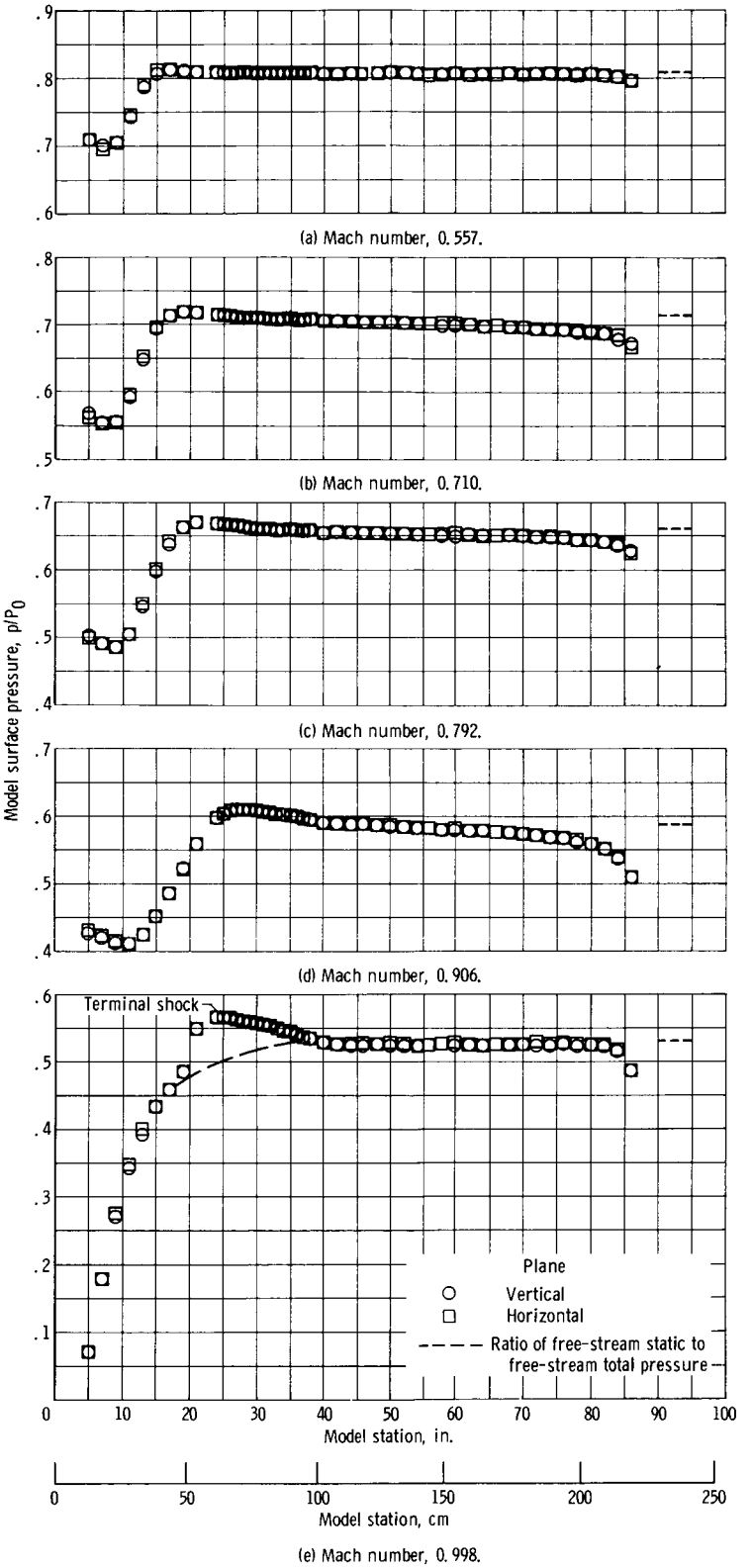

Figure 6. - Pressure distributions on 8-inch-diameter (20.32-cm-diam) 42° half-angle cone-cylinder model in 8-foot (2.44-m) - 3.1 percent porosity test section.

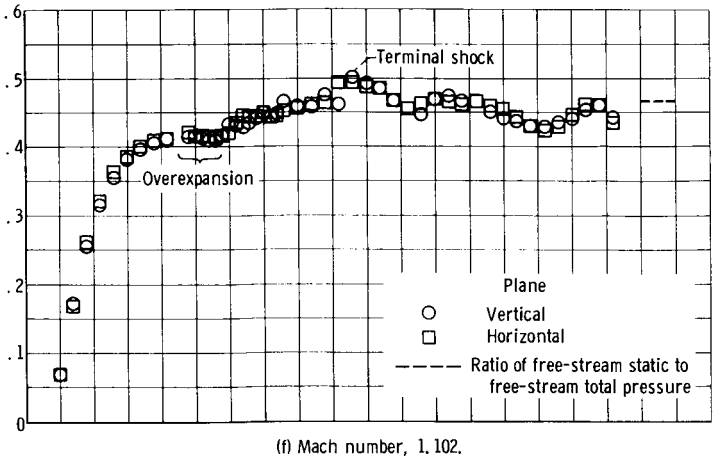

(f) Mach number, 1.102.

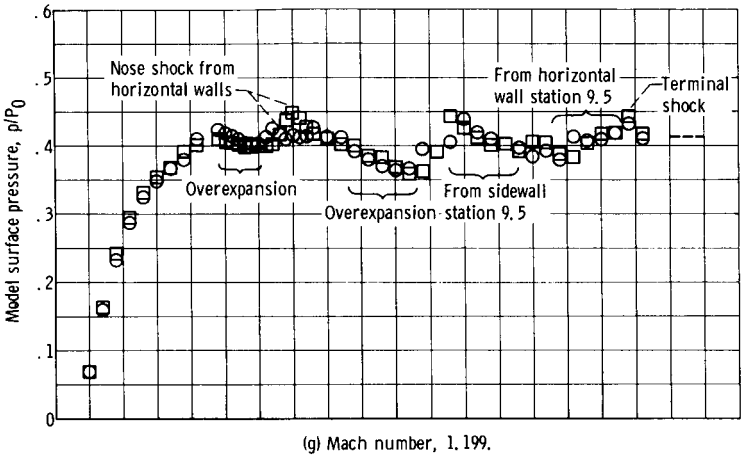

(g) Mach number, 1.199.

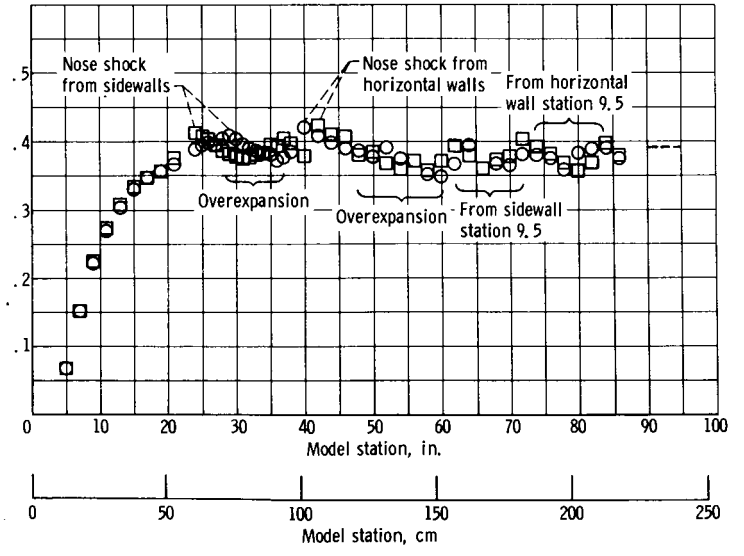

(h) Mach number, 1.241.

Figure 6. - Continued.

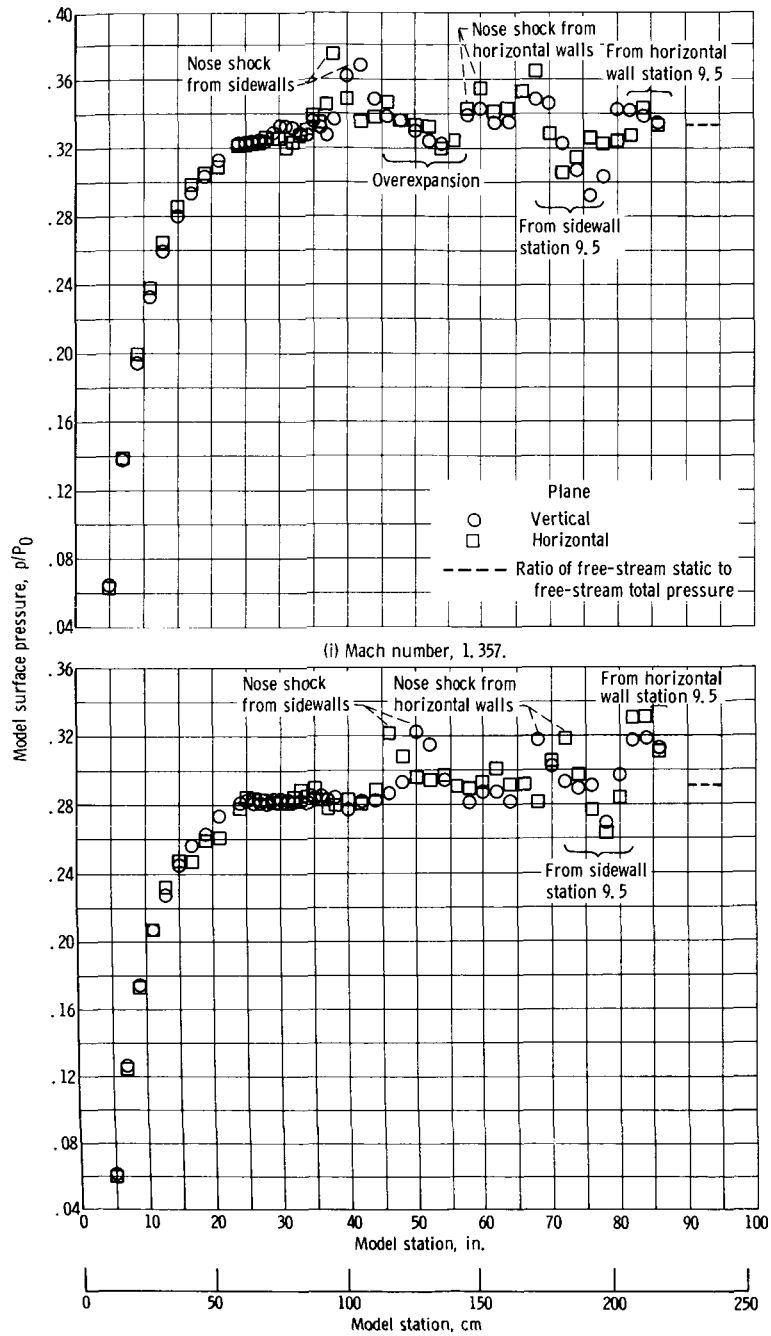

(i) Mach number, 1.357.

(j) Mach number, 1.454.

Figure 6. - Continued.

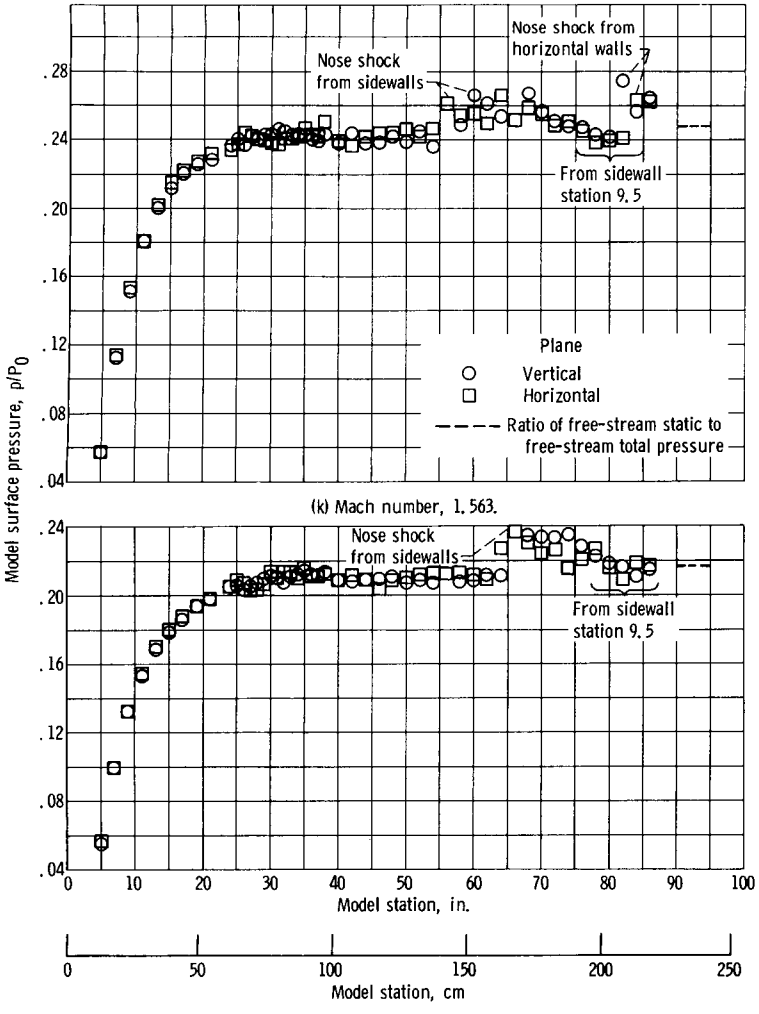

(k) Mach number, 1.563.

(l) Mach number, 1.656.

Figure 6. - Continued.

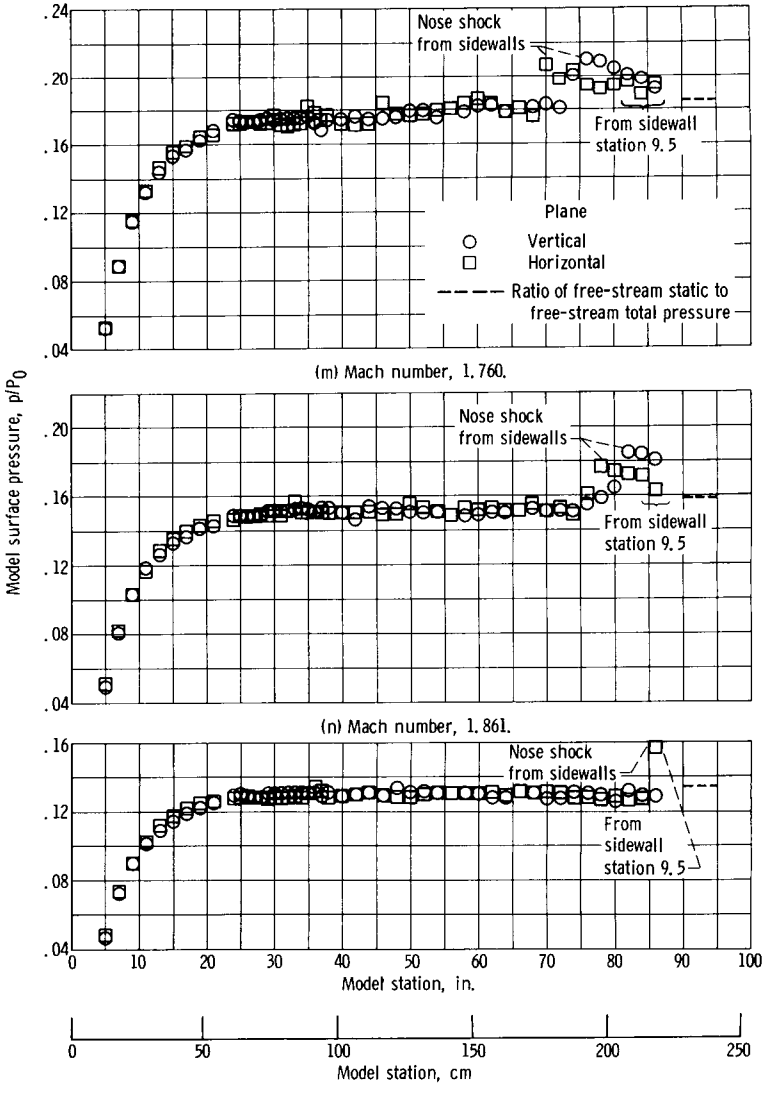

(m) Mach number, 1.760.

(n) Mach number, 1.861.

(o) Mach number, 1.968.

Figure 6. - Concluded.

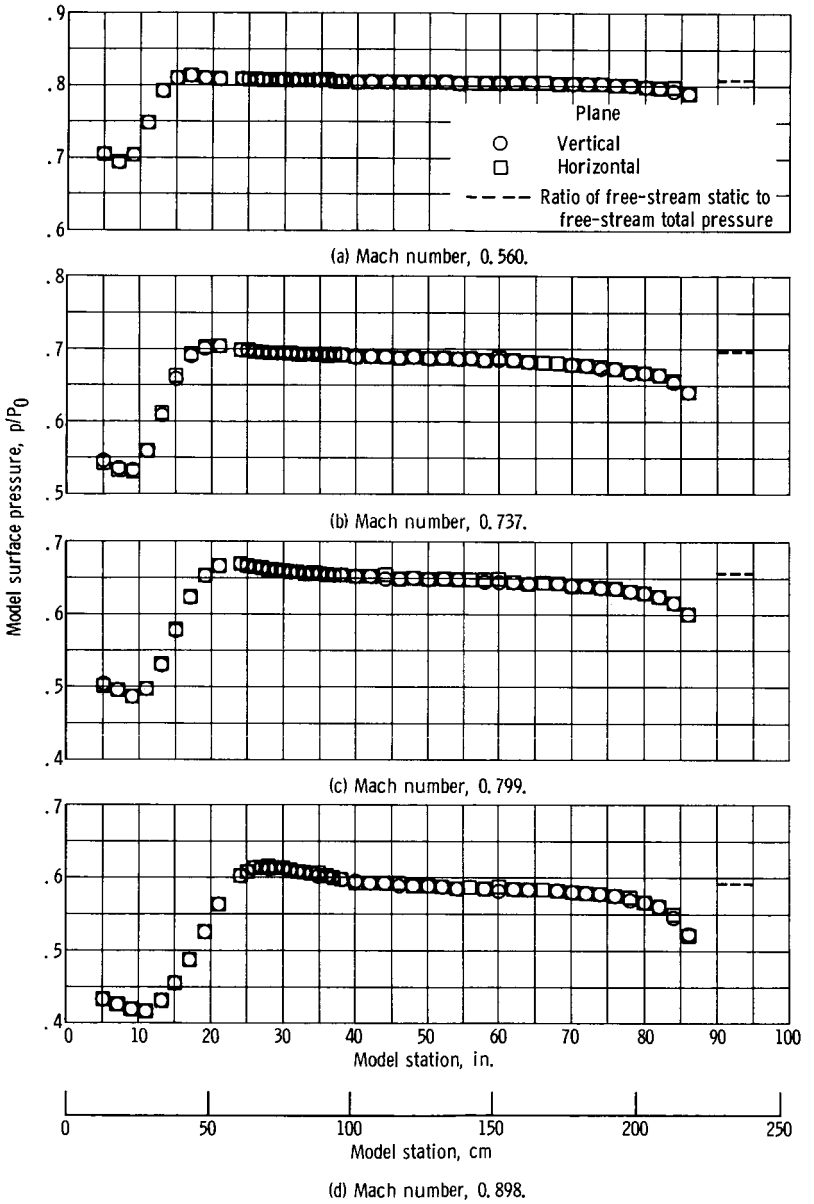

Figure 7. - Pressure distributions on 8-inch-diameter (20.32-cm-diam) 42° half-angle cone-cylinder model in 8-foot (2.44-m) - 6.2 percent porosity test section.

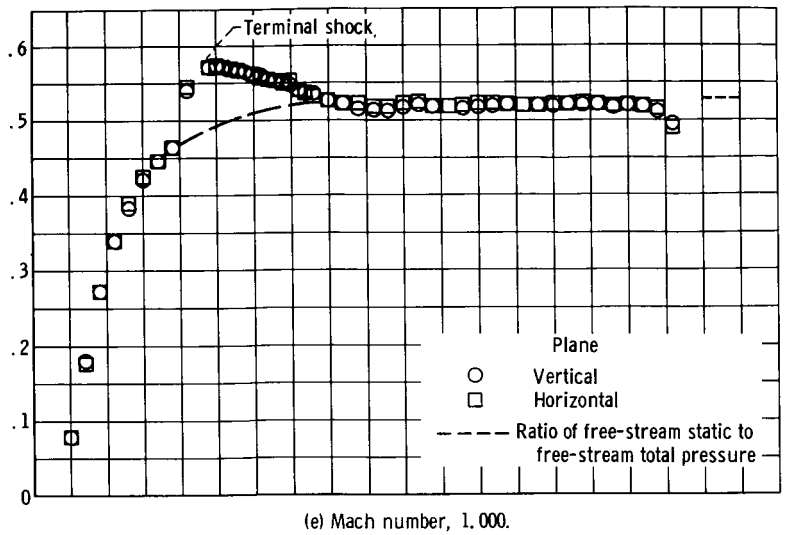

(e) Mach number, 1.000.

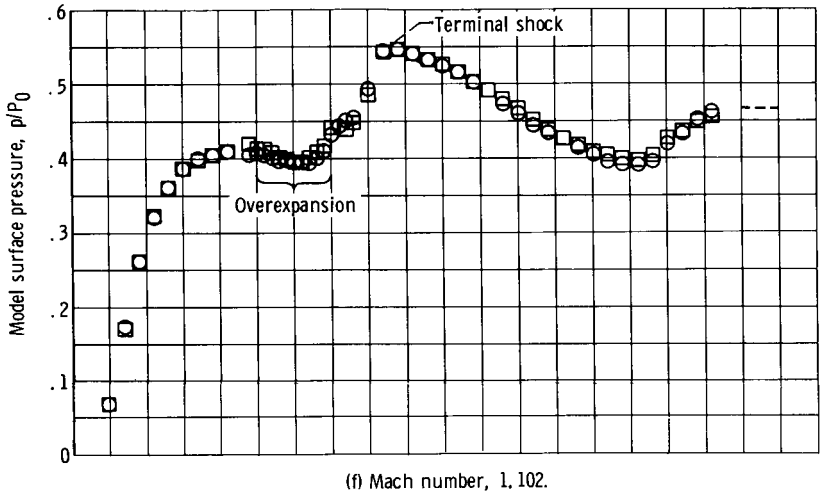

(f) Mach number, 1.102.

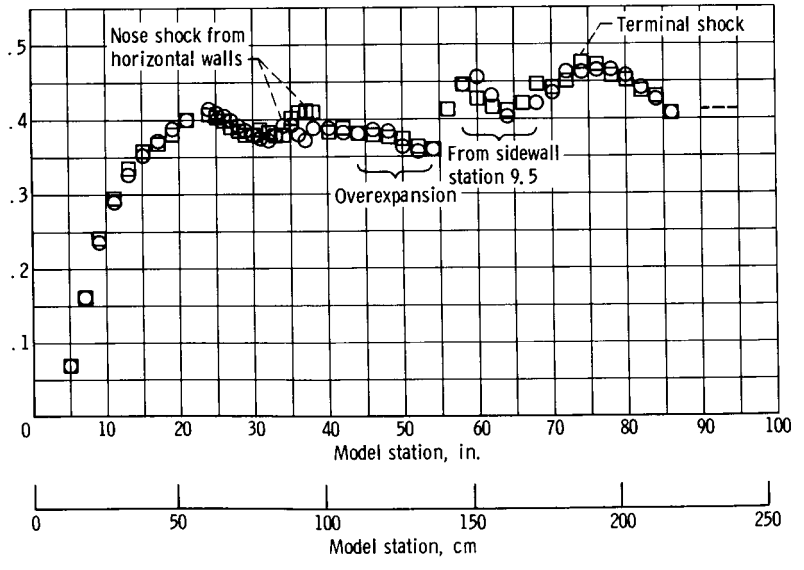

(g) Mach number, 1.199.

Figure 7. - Continued.

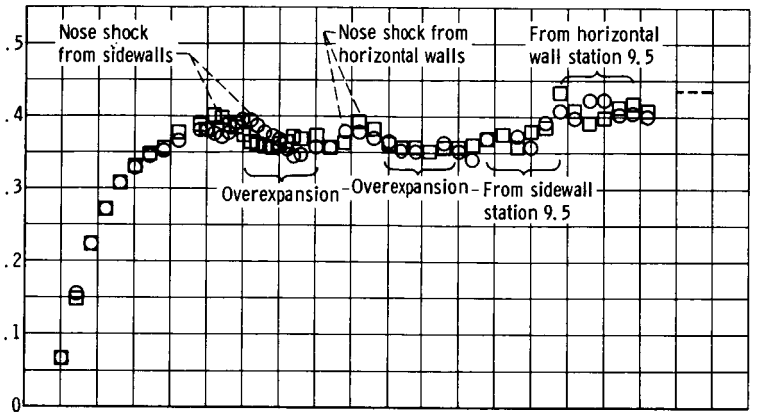

(h) Mach number, 1.253.

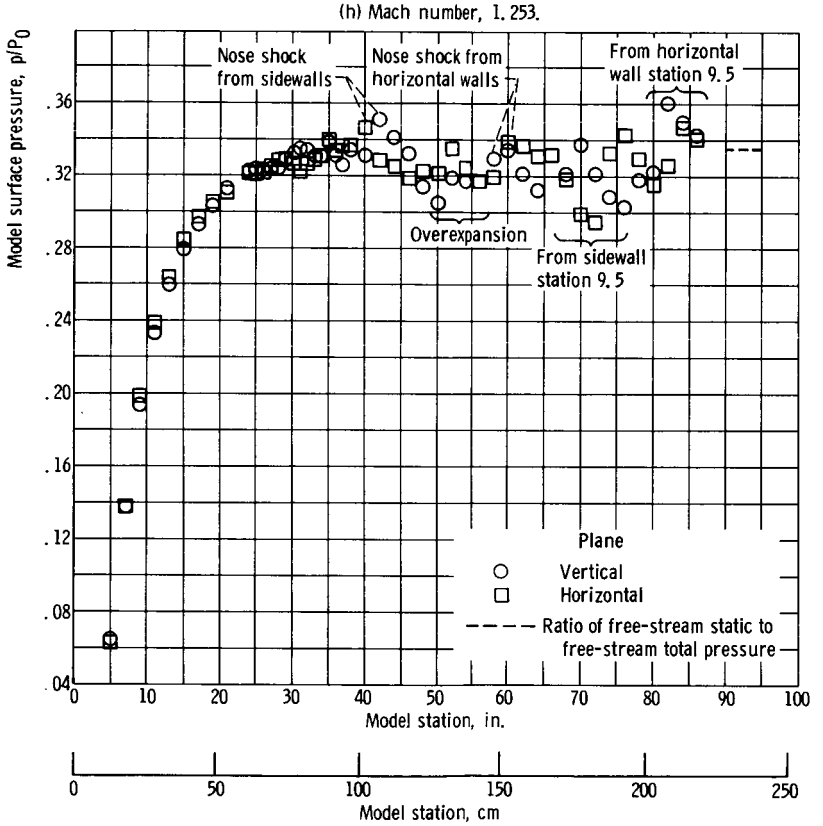

(i) Mach number, 1.353.

Figure 7. - Continued.

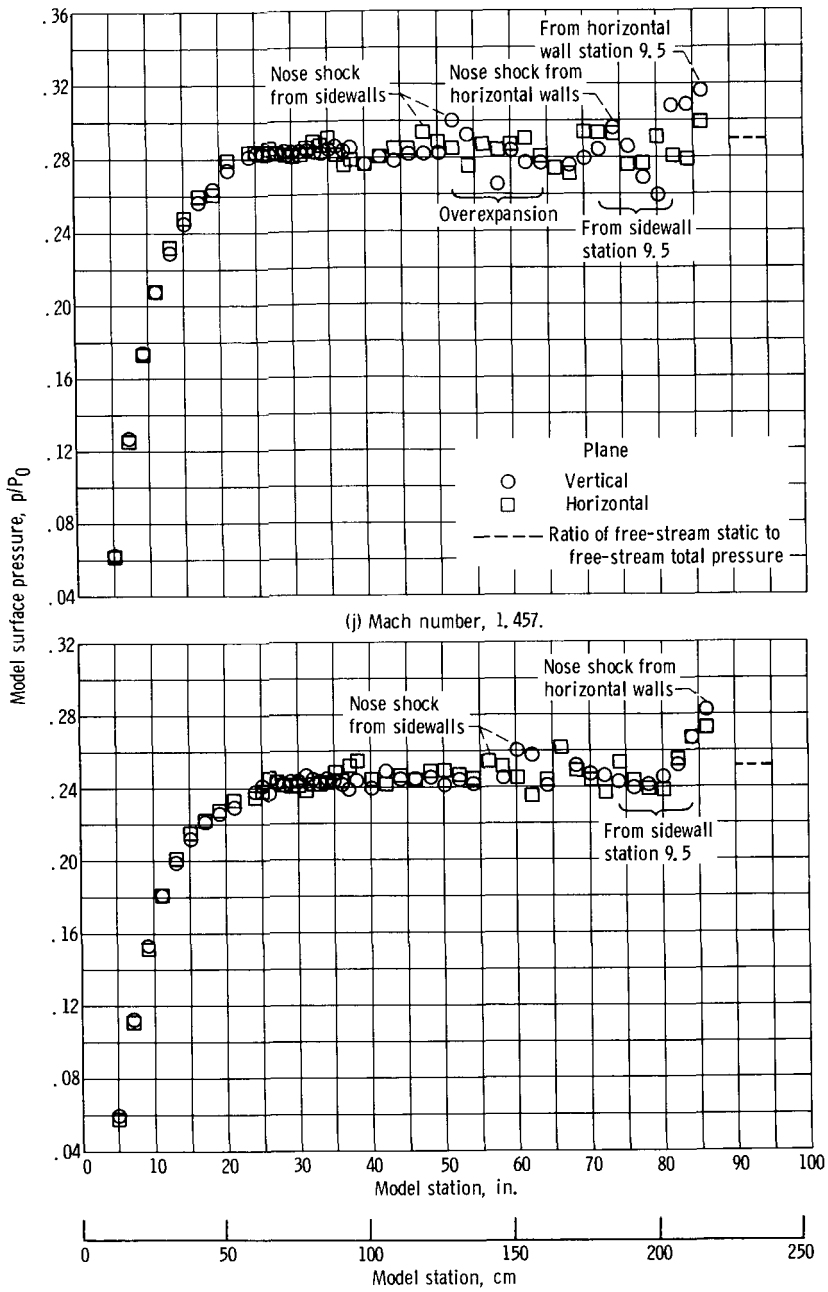

(j) Mach number, 1.457.

(k) Mach number, 1.555.

Figure 7. - Continued.

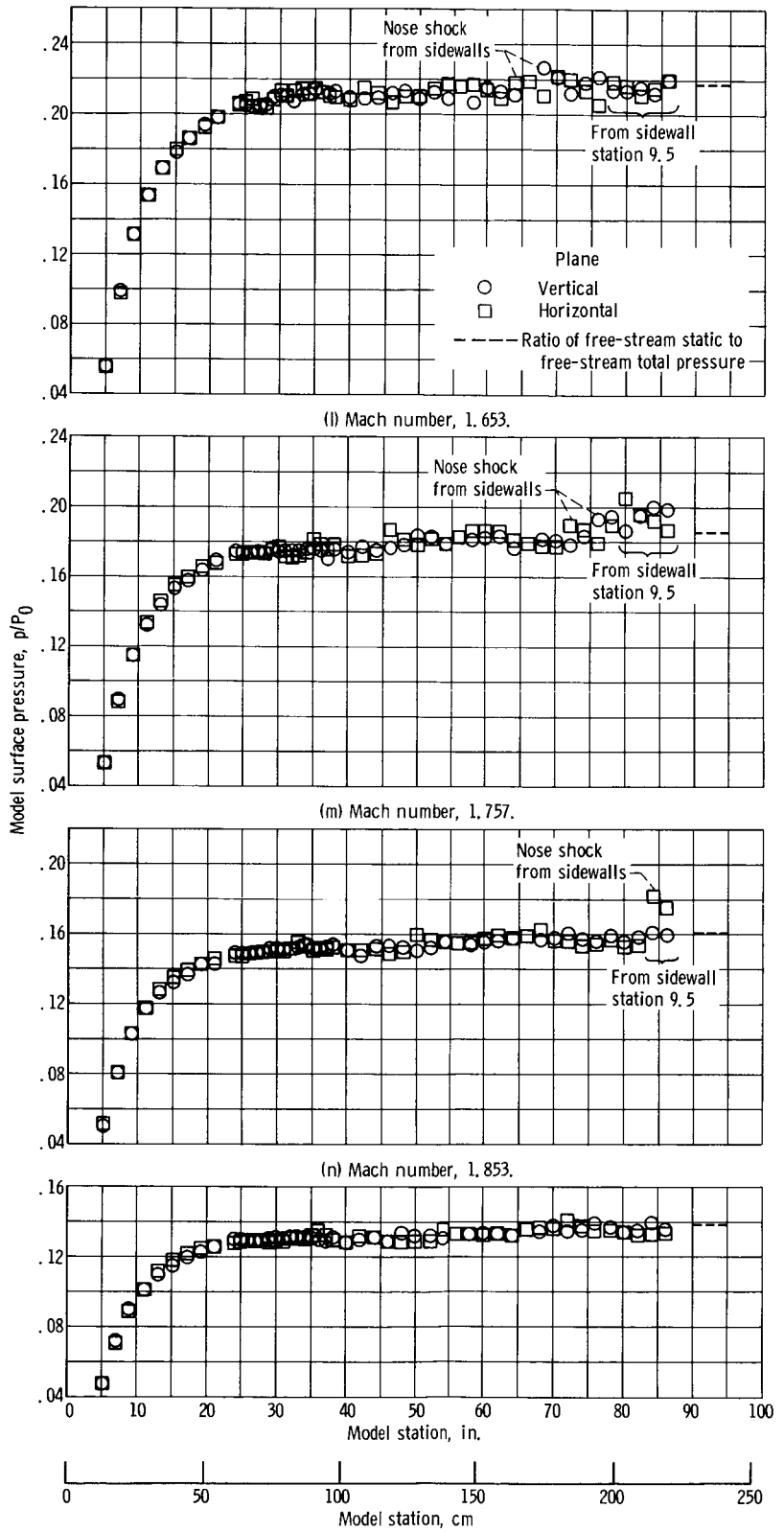

(l) Mach number, 1.653.

(m) Mach number, 1.757.

(n) Mach number, 1.853.

(o) Mach number, 1.948.

Figure 7. - Concluded.

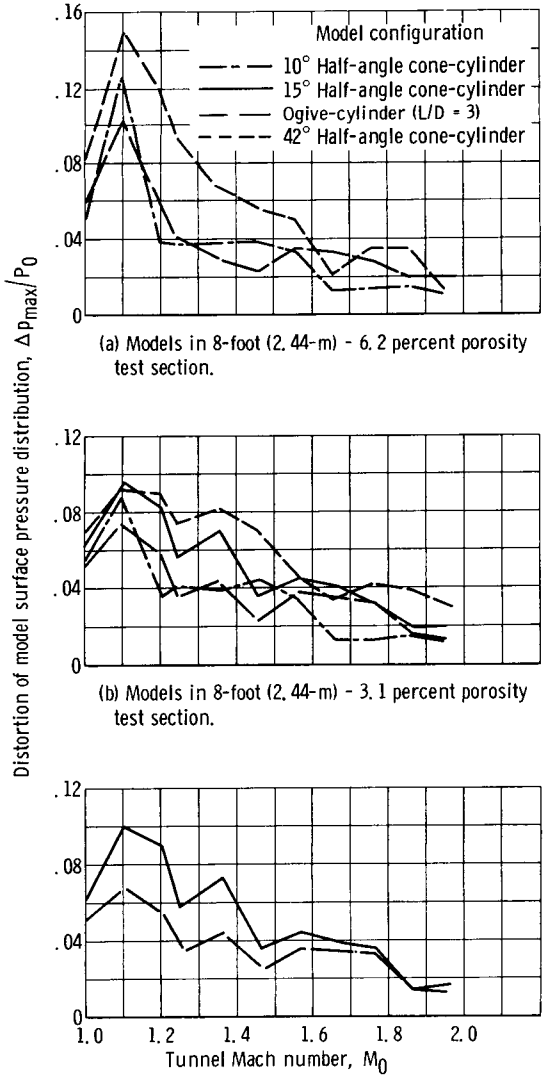

(a) Models in 8-foot (2.44-m) - 6.2 percent porosity test section.

(b) Models in 8-foot (2.44-m) - 3.1 percent porosity test section.

(c) Models in modified 8-foot (2.44-m) - 3.1 percent porosity test section.

Figure 8. - Effect of model shape on surface pressure distortion.

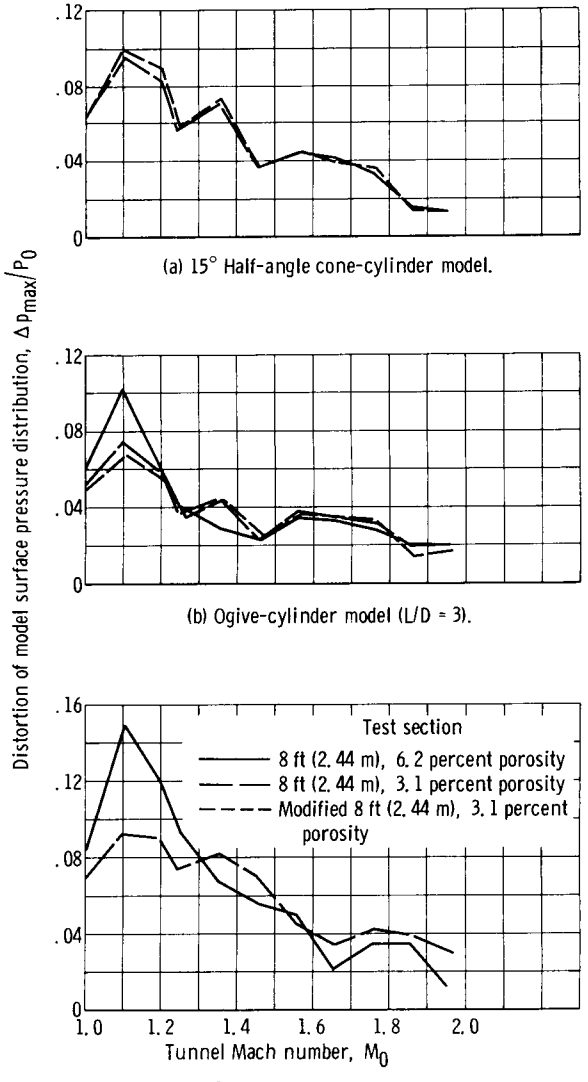

(a) 15° Half-angle cone-cylinder model.

(b) Ogive-cylinder model (L/D = 3).

(c) 42° Half-angle cone-cylinder model.

Figure 9. - Effect of test section configuration on model surface pressure distortion.

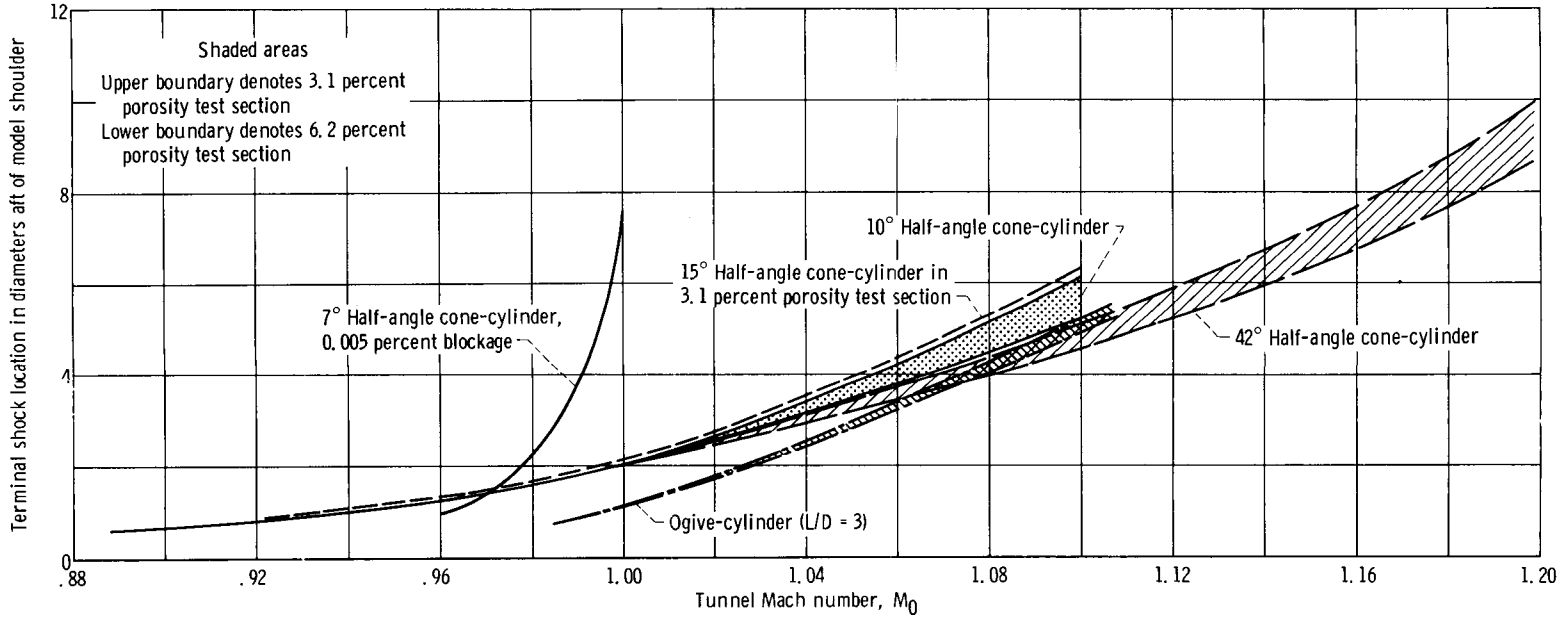

Figure 10. - Effect of model shape on terminal shock location.

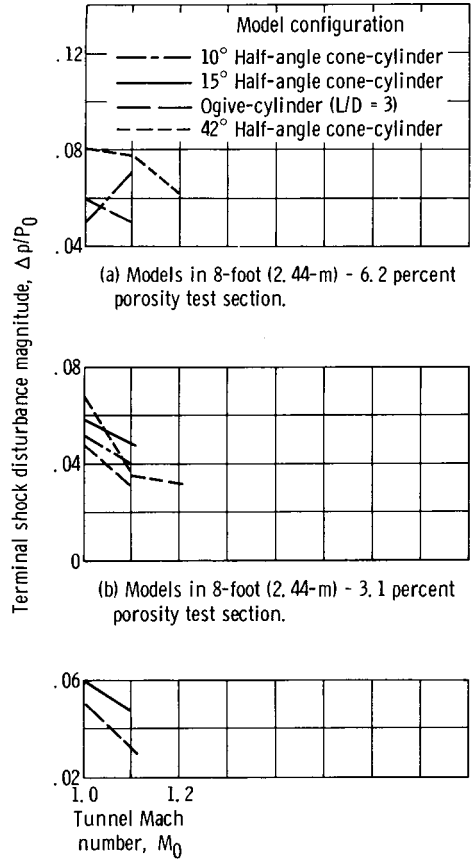

(a) Models in 8-foot (2.44-m) - 6.2 percent porosity test section.

(b) Models in 8-foot (2.44-m) - 3.1 percent porosity test section.

(c) Models in modified 8-foot (2.44-m) - 3.1 percent porosity test section.

Figure 11. - Effect of model shape on terminal shock magnitude.

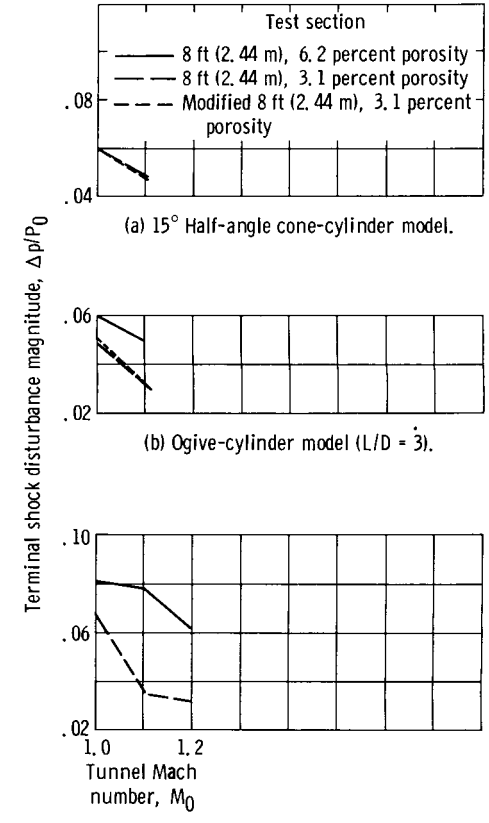

(a) 15° Half-angle cone-cylinder model.

(b) Ogive-cylinder model (L/D = 3).

(c) 42° Half-angle cone-cylinder model.

Figure 12. - Effect of test section configuration on terminal shock magnitude.

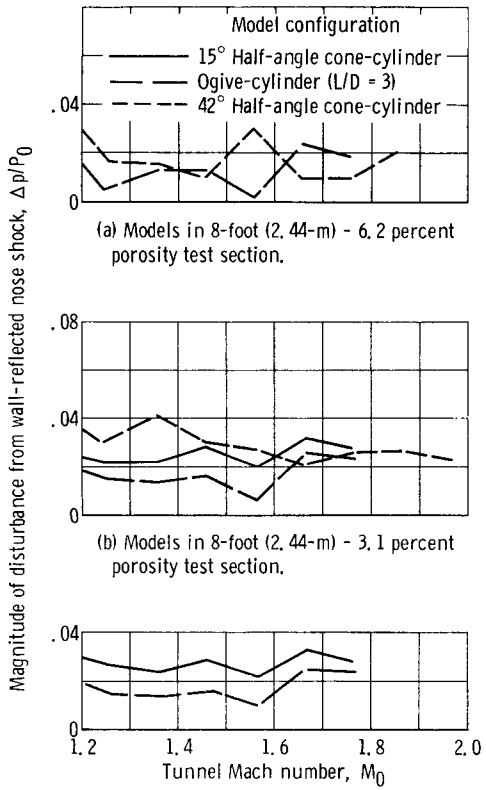

(a) Models in 8-foot (2.44-m) - 6.2 percent porosity test section.

(b) Models in 8-foot (2.44-m) - 3.1 percent porosity test section.

(c) Models in modified 8-foot (2.44-m) - 3.1 percent porosity test section.

Figure 13. - Effect of model shape on wall-reflected model nose shock.

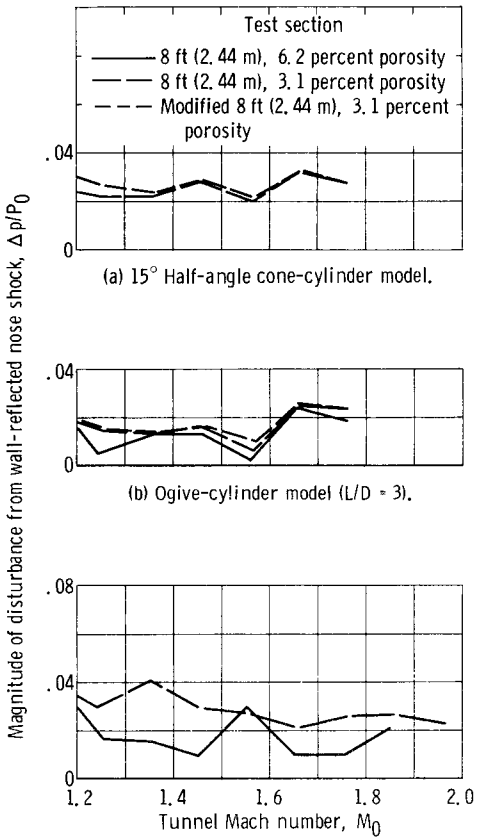

(a) 15° Half-angle cone-cylinder model.

(b) Ogive-cylinder model (L/D = 3).

(c) 42° Half-angle cone-cylinder model.

Figure 14. - Effect of test section configuration on wall-reflected model nose shock.

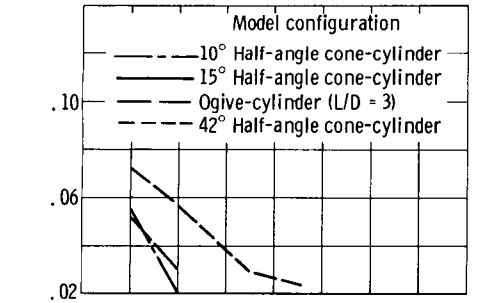

(a) Models in 8-foot (2.44-m) - 6.2 percent porosity test section.

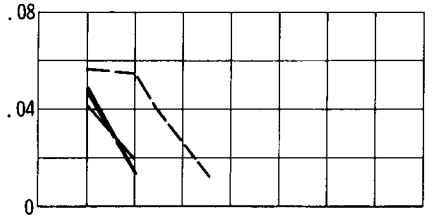

(b) Models in 8-foot (2.44-m) - 3.1 percent porosity test section.

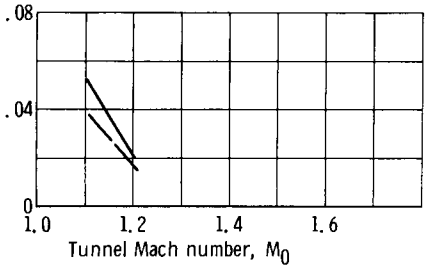

(c) Models in modified 8-foot (2.44-m) - 3.1 percent porosity test section.

Figure 15. - Effect of model shape on flow overexpansion.

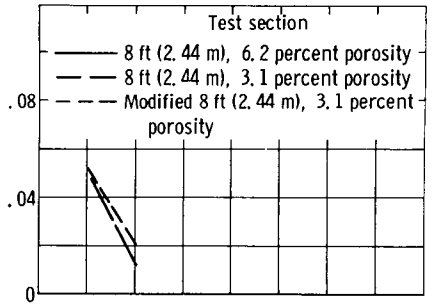

(a) 15° Half-angle cone-cylinder model.

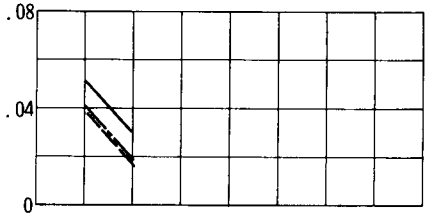

(b) Ogive-cylinder model (L/D = 3).

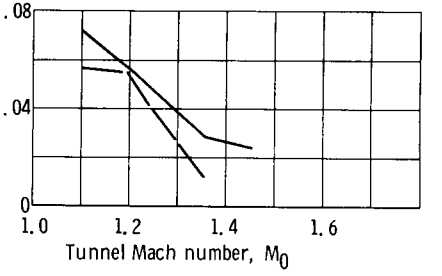

(c) 42° Half-angle cone-cylinder model.

Figure 16. - Effect of test section configuration on flow overexpansion.

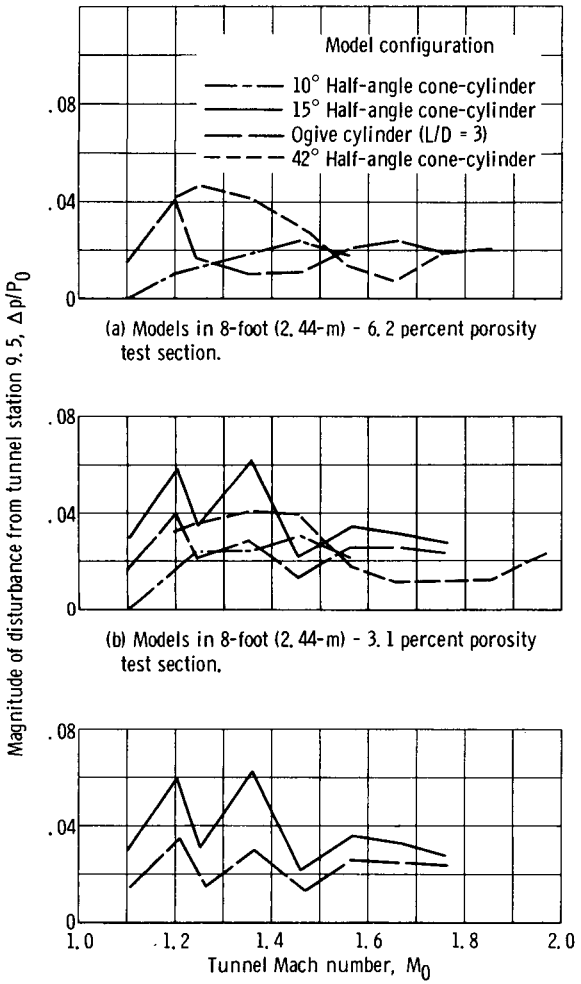

(a) Models in 8-foot (2.44-m) - 6.2 percent porosity test section.

(b) Models in 8-foot (2.44-m) - 3.1 percent porosity test section.

(c) Models in modified 8-foot (2.44-m) - 3.1 percent porosity test section.

Figure 17. - Effect of model shape on disturbance from tunnel station 9.5.

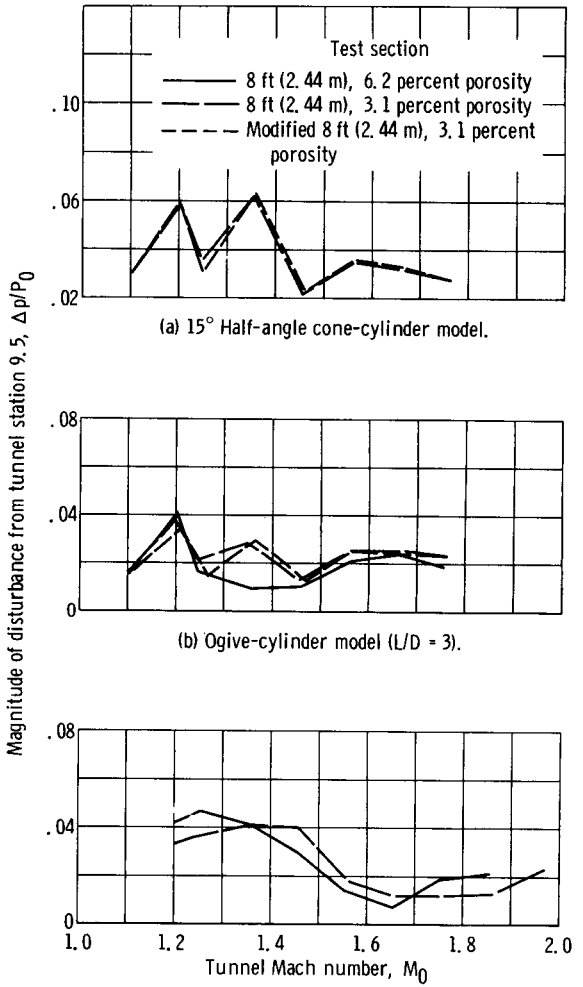

(a) 15° Half-angle cone-cylinder model.

(b) Ogive-cylinder model (L/D = 3).

(c) 42° Half-angle cone-cylinder model.

Figure 18. - Effect of test section configuration on disturbance from tunnel station 9.5.

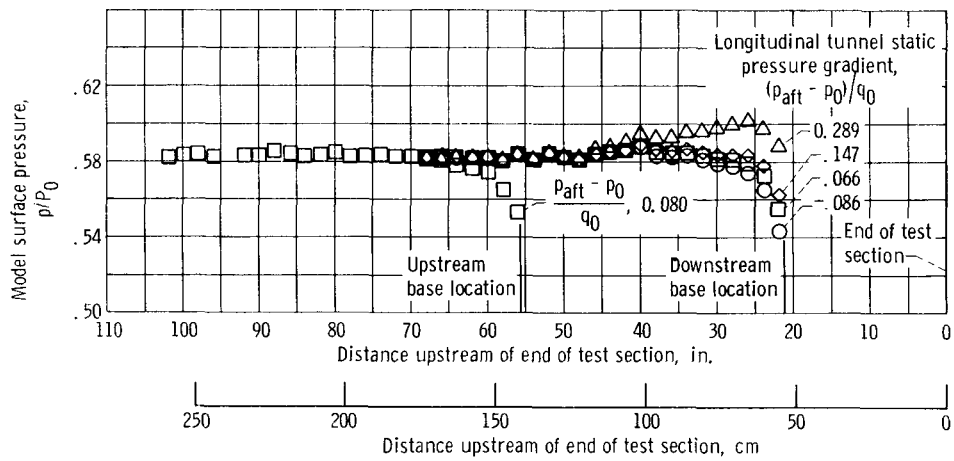

Figure 19. - Aft model pressure distributions at two model base locations. Tunnel Mach number, 0.9.

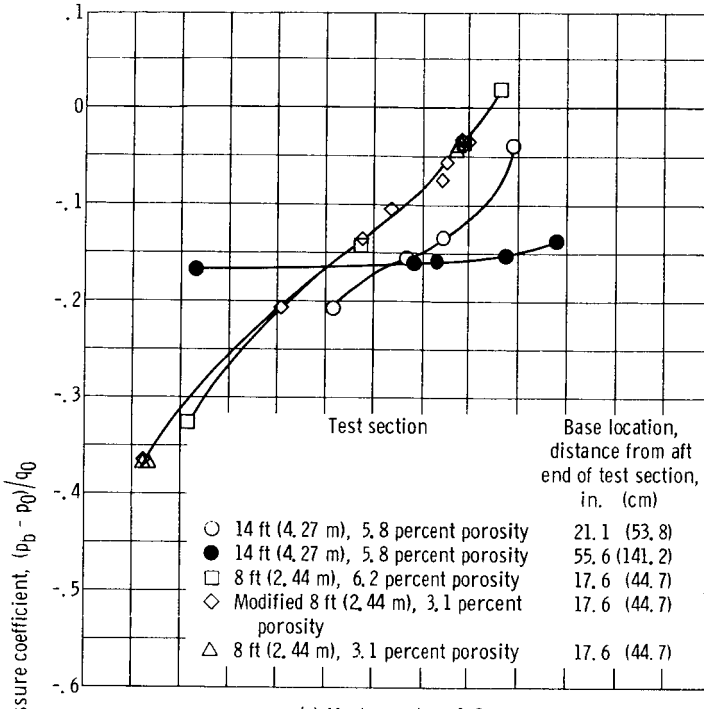

(a) Mach number, 0.9.

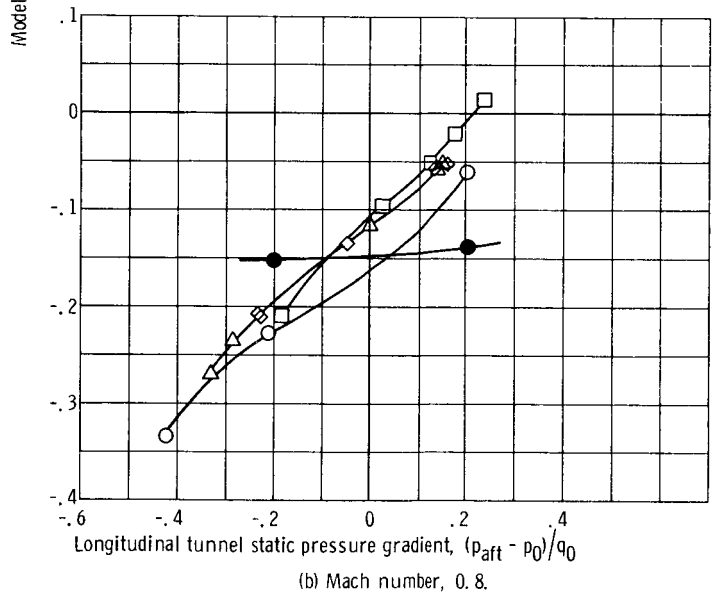

(b) Mach number, 0.8.

Figure 20. - Base pressures for 8-inch (20.32 cm) model.

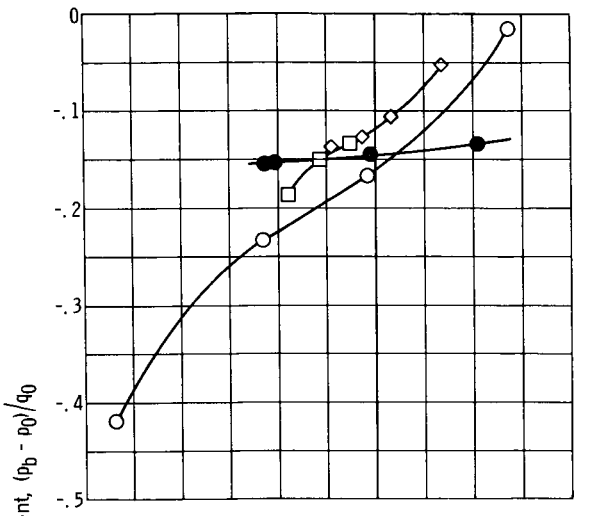

(c) Mach number, 0.7.

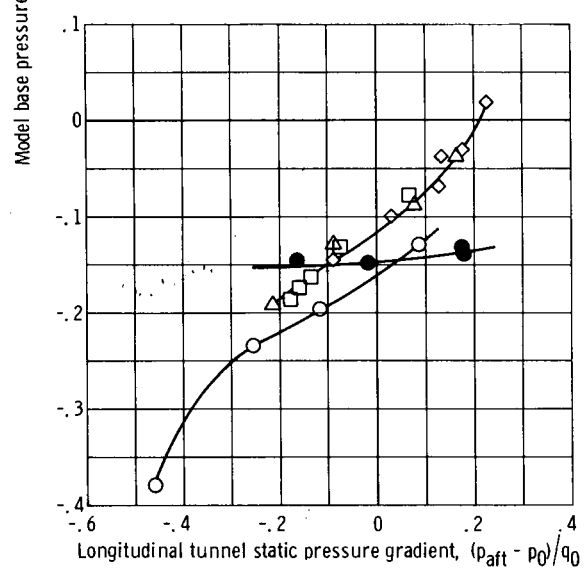

(d) Mach number, 0.56.

Figure 20. - Concluded.

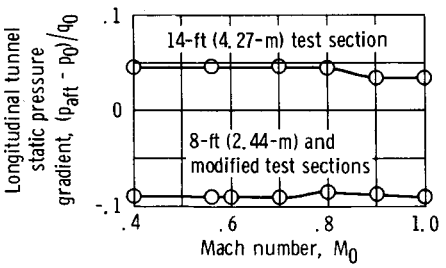

Figure 21. - Recommended longitudinal tunnel static pressure gradient for subsonic Mach numbers.

NASA-Langley, 1968 — 1 E-4400